5-2021

Testing Methods of Surficial Sinkhole Identification Using Remotely Sensed Data

Dane P. Brophy
Utah State University

Testing Methods of Surficial Sinkhole Identification Using Remotely Sensed Data

by

Dane P. Brophy

A project report submitted in partial fulfillment

of the requirements for the degree

of

MASTER OF SCIENCE

in

Civil and Environmental Engineering

Approved:

_____	_____
Bethany Neilson, Ph.D. Major Professor	David Liddell, Ph.D. Committee Member
_____	_____
Ruijie Zeng, Ph.D. Committee Member	Richard Cutler, Ph.D. Interim Vice Provost for Graduate Studies

UTAH STATE UNIVERSITY
Logan, Utah

2021

Contents

List of Tables

List of Figures

Abstract

Nearly a quarter of all people rely on karst aquifers for drinking water. In the United States, the Safe Water Drinking Act requires a complete assessment of public water systems' vulnerabilities to contamination. As part of that assessment, watershed boundaries must be delineated, while recharge and supply locations identified. In the context of karst aquifers, surficial karst features, such as sinkholes, can act as a point source of direct recharge to karst aquifers and create vulnerabilities to critical drinking water sources. Historical methods of locating these features are inefficient and depend on basic field investigations, resulting in a clear need for advanced identification methods. To this end, this study focuses on developing more efficient identification methods that use remotely sensed data to locate and map surficial karst features that may require protection. Satellite and unmanned aerial vehicle (UAV) data were used to explore the resolution needed to identify surficial karst feature signatures and the most promising methods for analyzing these data. This study's data included red, green, blue, and near-infrared reflectance rasters, thermal mosaics, and digital surface and terrain models. Spectral and thermal properties were used to filter data that could include karst features. Additionally, digital elevation models were used to explore multiple smoothing methods, image differencing, edge detection, terrain curvature, sink location, and watershed delineation. Findings from the different methods were compared to known karst feature locations. Data with a resolution between 0.5 and 2.5 meters per pixel were found to be ideal for most methods tested. However, vegetation removal, followed by a simple interpolation to fill these areas, created data analysis problems and highlighted the need for other data products, such as LiDAR, that provide accurate elevations of terrain shrouded by vegetation. In the end, it was found that edge detection, mapping curvature, and locating of low points (or sinks) via DEM analyses are all promising methods. It was concluded that by combining multiple methods, detailed digital terrain models could accurately locate many surficial karst features.

Acknowledgments

Everyone should be lucky enough to have a person in their life that believed in them, gave them a chance, and changed them for the better; for me, that person is Dr. Bethany Neilson, my Major Professor. I was fortunate enough to meet Dr. Neilson while completing my undergraduate degree. Since that time, she has mentored me and helped me understand how I could become more successful. I am very grateful she took the time to invest in me and help me get to where I am now. Next, I would like to thank Dr. David Liddell and Dr. Ruijie Zeng, both of whom are members of my committee. Dr. Liddell has been vital in shaping my overall geologic understanding and has always been willing to discuss my questions and rock specimens. Dr. Zeng has spent much time on this project instructing me, discussing image processing methods, troubleshooting scripts, and offering advice. This project would not have been possible without the help and guidance of these three people. I wholeheartedly express my gratitude for their time, patience, and dedication to education.

Other people who have been a valuable resource and have assisted me through the process of completing my project include Ian Gowing, Dr. Jeffery Horsburgh, Dr. Douglas Ramsey, Patrick Strong, Shannon Syrstad, Dr. David Tarboton, and Dr. Alfonso Torres-Rua. Throughout this project and my time at USU, I have always had a network of people willing to offer me advice and direction on my academic endeavors. I also want to express my gratitude for people who were there as a friend, a listening ear, or a support throughout my time as a student. Those people include Andrea Carroll, Eileen Lukens, Bryce Mihalevich, Hyrum Tennant, and Mindy Whiteley. I feel fortunate to have had these individuals in my corner through this challenging adventure.

I would also like to thank my beautiful wife, Lilly Brophy, and my loving children; Lila, Niles, Emalise, and Alannah. They have been patient with the long hours required to complete my degrees, been happy to make due with what we had, always been good for a hug and comfort, and have been a constant source of encouragement along the way. Finally, I would like to thank my mother, Peggie Quinn. No matter what it was, she always believed I could; she taught me to see through limitations placed on me and look to the future while learning from the past. These individuals were my motivation to pursue my degrees, the support I needed to complete them, and the biggest reasons that I am where I am today.

Thank you all.

Introduction

Ford and Williams (2007) estimate that soluble rocks suitable for developing karst networks cover as much as 10 – 15% of Earth's surface. Karst aquifers are an essential water resource throughout the world and supply water for various uses, including drinking, irrigation, and power supply (Goldscheider, 2005). Additionally, Ford and Williams (2007) estimate that as much as 20 – 25% of the global population may be relying on karst aquifers as a source of drinking water.

In 1996, the Safe Water Drinking Act (SDWA) was amended by Congress and required all states to compile and submit Source Water Assessment Plans (SWAPs) (Ginsberg and Palmer, 2002). These SWAPs required a complete assessment of public water systems, including boundary delineations of water supply locations. Ginsberg and Palmer (2002) explain that karst aquifers are extremely susceptible to contamination from pollutants, which once in the aquifer can spread rapidly. This is due to karst systems containing multiple porosity types, including micropores, small fissures and fractures, and large fractures and conduits (Hartmann et al., 2014). These subterranean waterways widen and link together with continued flow along bedding planes, through fractures, and within existing dissolution features (Ewers, 1982; Ginsberg and Palmer, 2002; Hartmann et al., 2014). This combination of porosity types and continuing maturity of karst networks increases hydraulic conductivity and decreases residence time (Goldscheider, 2005; Palmer, 2007). Additionally, a karst aquifer with mature flow paths can experience limited pollutant filtration and increased potential for transport (Ginsberg and Palmer, 2002). Karst aquifers experience recharge from both diffuse and point sources (Goldscheider, 2005). Though most water enters karst aquifers through bedding planes and fractures, dissolution features, such as sinkholes, are a point source for recharge to the aquifer (Ginsberg and Palmer, 2002). That knowledge illustrates the need to locate these vulnerable recharge areas that allow for direct contribution of pollutants into karst aquifers.

Understanding the interaction of karst features and aquifers is also essential because of their vast storage and ability to quickly transmit water. Because karst aquifers receive more recharge, and both store and transmit larger volumes of water (Kresic, 2013), it becomes clear that an improved understanding of underground reservoirs and conduits within karst features would result in an ability to quantify groundwater stores. It would also help discover how the anticipated shifts from a snow-dominated system to a rain-dominated system across the Intermountain West will affect our water resources (Tyson, 2021). Before a better understanding of conduits and subsurface connections can be gained, surface karst features, primarily fractures and sinkholes, must be mapped. However, surficial karst features can be hard to locate due to terrain, remoteness, and vegetation cover.

Utah's Bear River Range includes the Logan River watershed, where the canyon portion of the watershed is comprised of formations consisting primarily of carbonates with some units of quartz-cemented quartz sandstone (Bahr, 2016). One prominent feature of these units is a large number of karst features, such as sinkholes and cave structures, which act as subsurface drainage networks (Spangler, 2011). Water from these karst networks drain to the Logan River and is used to generate electricity and irrigate agricultural lands across Cache Valley and urban areas within Logan City. The karst networks and aquifers also provide drinking water to surrounding areas.

Spangler (2011) used dye tracing to measure flow-through rates of the karst drainages and mapped the pour points of some of the more prominent karst features within Logan Canyon. Additionally, through groundwater chemical signatures, Spangler was able to suggest that the rocks through which the conduits run have notable differences. Bahr (2016) focused on mapping the karst features in the locale of Tony Grove to study how structures within the geology affected the karst complexes. Bahr showed that these mountainous karst systems are "highly influenced" by the orientation, geometry, permeability, and deformation of the rock units in which they are located. More

recent work has focused on the connections between groundwater recharge and river and spring discharge changes throughout the watershed (Neilson et al., 2018). They documented significant gains and losses of water volume over expanses of the river channel that are primarily sourced by low residence time, karst conduit water. Recent, ongoing efforts are trying to relate snow accumulation and melt patterns to baseflow in the river (Tyson, 2021). However, these efforts do not account for sinkhole locations where the karst terrain plays a major role in water delivery to the river throughout the year.

Given the importance of the karst aquifer to the future of Cache Valley's water, there is a clear need to further understand karst aquifer recharge and discharge. A critical component of this future work is identifying primary recharge locations and, in particular, sinkholes. Based on the size of karst features in the Bear River Range and the relatively small amount of vegetation, it was hypothesized that remote sensing methods could be used to provide a method for detecting sinkholes or openings into karst groundwater systems. To test that hypothesis, this study utilizes remotely sensed data in the form of satellite and UAV spatial data that has been geo-located. The satellite data was used in an attempt to visually identify anomalies amongst known karst features and test the resolution of available data to see if it is sufficient to move forward with additional analysis of data. Data collected by UAV provided spectral imagery in red, green, blue, and near-infrared wavelengths; an elevation model; and thermal imagery of the ground surface. Analysis performed on these data include calculating vegetation indices, limiting data based on a spectral survey of vegetation, and filtering data based on a thermal survey of known karst features. Efforts to identify karst signatures applied methods including image differencing, edge detection, and curvature calculations. Identification of surficial karst locations using watershed delineation and sink identification was also explored. Because the UAV collected data had an extremely fine resolution, appropriate data resolution requirements for future studies were also investigated. In the end, this study succeeded in identifying promising methods for locating surficial karst features that should be further investigated.

Methods

This study focuses on a location in the canyon portion of the Logan River watershed situated approximately 20–25 km east–northeast of Logan, UT. Logan Canyon is located in northern Utah's Bear River Range and is the consequence of Cretaceous west-to-east thrusting during the Laramide orogeny (Spangler, 2011). The Logan River is a third-order river that flows west-southwest with a snow-melt-dominated hydrograph (Neilson et al. 2018). The watershed includes coastal deposits that were materialized during the Paleozoic era, with most of the deposition between the Ordovician and Devonian periods (Spangler, 2011). Given the need to establish an identifiable signature of karst features, the study area in Logan Canyon has 80 horizontal and vertical karst features already identified (Figure 1). Data gathered for this study included high-resolution satellite data and higher resolution UAV survey data to test different feature identification methods (Table 2).

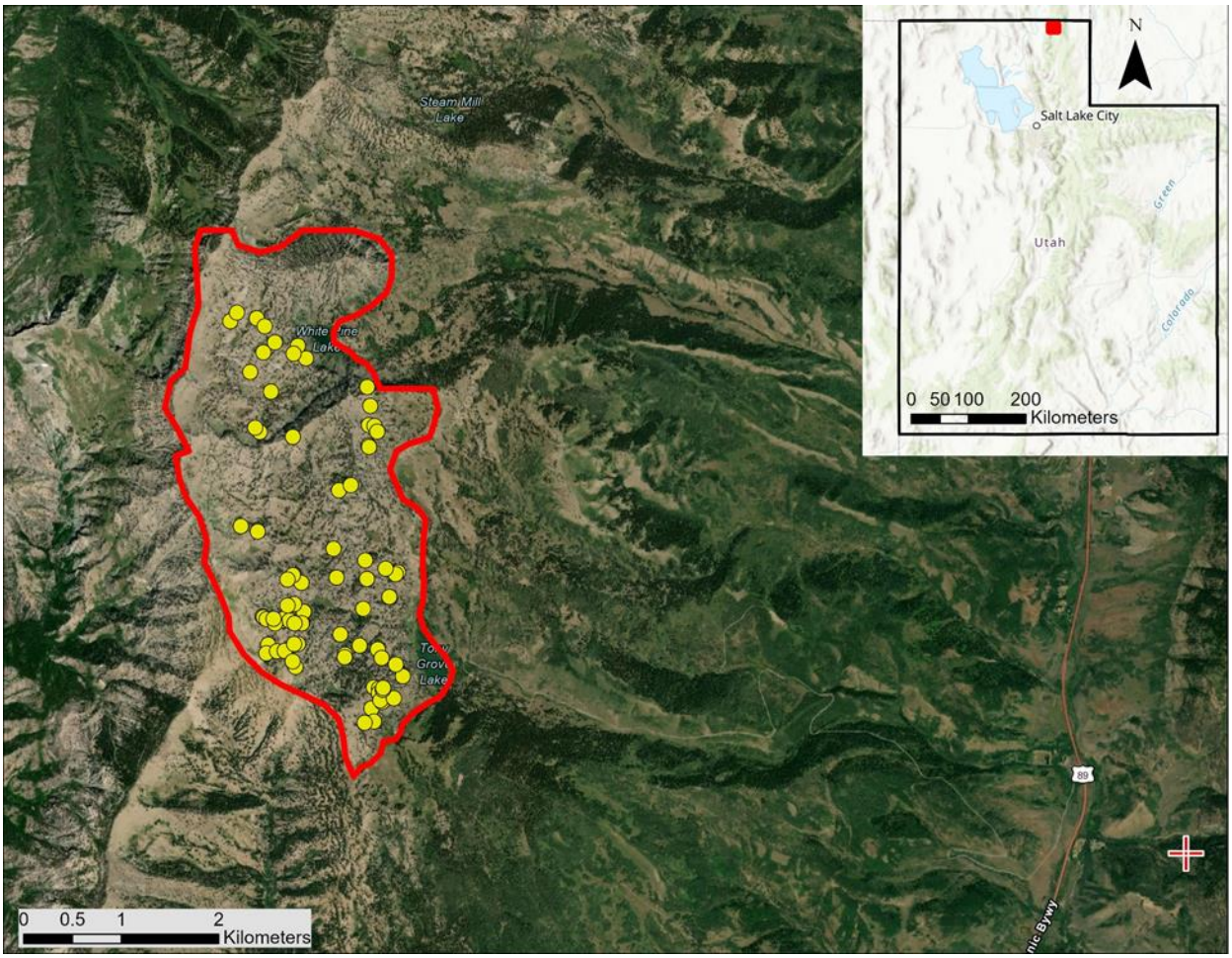

Figure 1: Study area (red polygon) with known karst locations (yellow points) used with satellite data. These karst locations include both vertical and horizontal dissolution features. The Tony Grove Climate site location, used for relative humidity and temperature data, is also noted as a red cross.

Remotely Sensed Data

Remotely sensed data products, and altered versions of those products (Table 2), were used to complete initial analyses. Satellite data were downloaded from Planet, a private company founded in 2010, consisting of Red Green Blue (RGB) and Near Infrared (NIR) RapidEye Analytic Ortho Tile data, at a resolution of 3 – 5 meters per pixel (Planet Team, 2017). Additionally, a UAV survey was completed on September 29th, 2019, between 9:00 AM and Noon, by USU's AggieAir for two areas of interest. The location of these surveys was based on the density of known surficial karst features, hereafter referred to as Polygon 1 and Polygon 2 (Figure 2). An octocopter (Matrice 600 Pro) was equipped with both RGB-NIR and thermal imaging sensors and was flown in a detailed zig-zag pattern to collect high-resolution

data for these areas (Figure 3). The purpose of the UAV flights was to provide fine spatial resolution data to test methods for identifying signatures common amongst karst features and assess data resolution requirements for future studies.

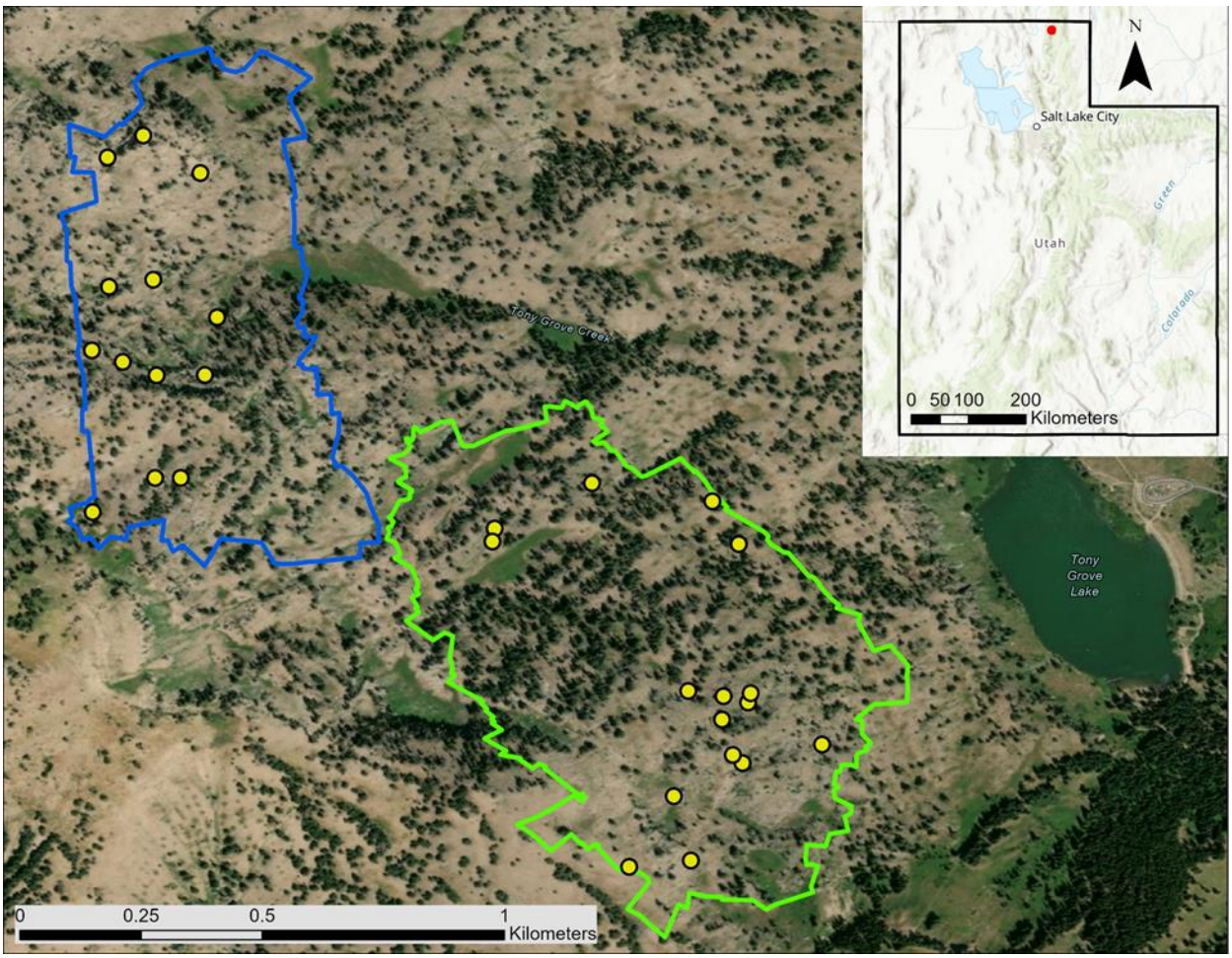

Figure 2: Extent of UAV study; resulting from data collected following AggieAir UAV flight. Polygon 1 in green, Polygon 2 in blue, and known karst features in yellow.

UAV:	Matrice 600 Pro
Coverage Area:	0.75 mi^2
Range:	4 mi
Airtime:	30 min
Payload:	5 lbs
Max Weight	32 lbs
Frame Size:	600 mm
Sensors:	Resolution:
RGB-NIR	2 cm
Thermal	15 cm

Figure 3: Specifications of the Matrice 600 Pro octocopter, which conducted the UAV flight (https://uwrl.usu.edu/aggieair/uav-service-center/platforms-sensors).

Reflectance data obtained from the UAV flight consists of RGB and NIR data. That data was combined into a single dataset to make a single reflectance layer with a resolution of about 2.3 cm per pixel (Figure 4, Table 2). The resulting 4-band reflectance mosaics has band 1 containing the red wavelengths, band 2 covering the green wavelengths, band 3 the blue wavelengths, and band 4 the Near Infrared (NIR) wavelengths (Table 1). However, for much of this work, the reflectance layer is presented as a false-color composite (e.g., Figure 5a), where the color red has the NIR input, the green layer has the red input, and the blue layer has the green input (Figure 5a).

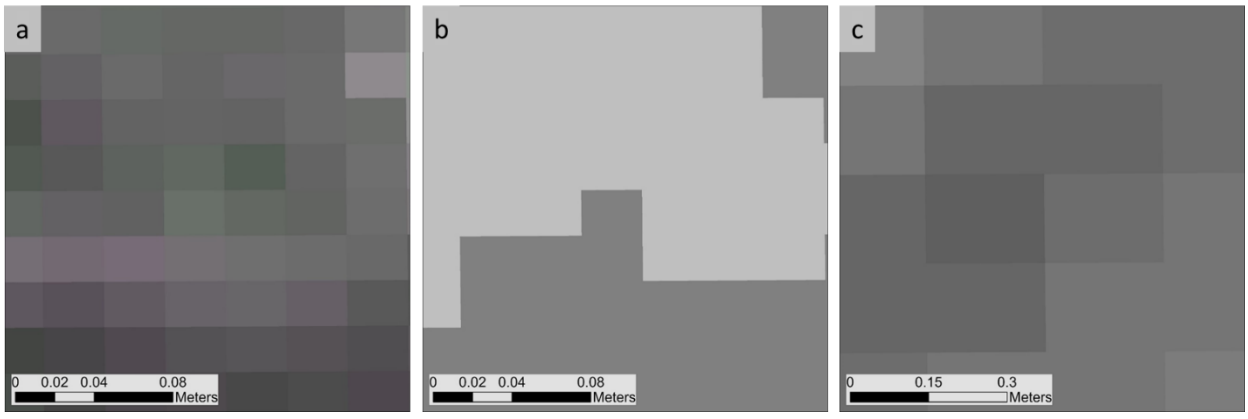

Figure 4: Resolution of UAV-based spectral imagery (a), digital surface model/digital terrain model (b), and thermal raster (c).

Table 1: Association between UAV bands within the 4-band reflectance layer and the colors those bands represent.

Reflectance Layer Bands				
Band	1	2	3	4
Reflectance	Red	Green	Blue	NIR

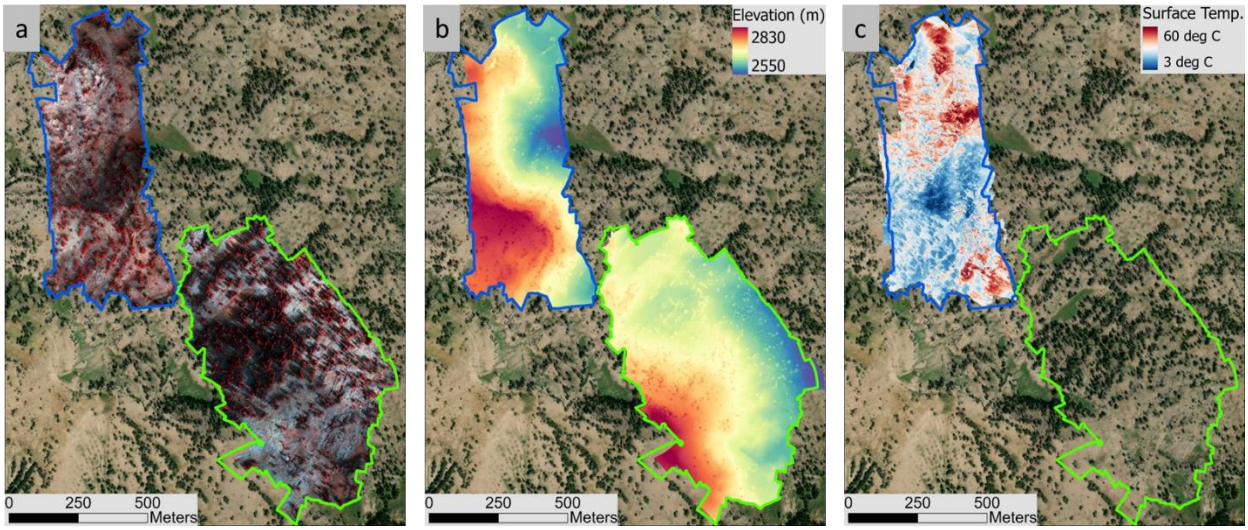

Figure 5: Raw data obtained through UAV flight. False-color composite of spectral imagery (a), digital surface model (DSM) displaying elevation (b), and thermal data showing the uncalibrated temperature in Celsius (c). Note thermal imagery not processed for Polygon 1.

AggieAir technicians utilized the UAV reflectance data and Agisoft Metashape Professional software (Agisoft) to produce a Digital Surface Model (DSM) at a resolution of 2.3 cm per pixel (Figure 4 and 5, Table 2). The process was completed by building a dense point cloud from UAV-collected imagery and assigning a calculated elevation for each pixel within the image. That data was then orthorectified to create the DSM for each polygon (Figure 5). Utilizing the resulting DSM from each polygon, a Digital Terrain Model (DTM) was then created (Table 2). The difference between a DSM and a DTM is simply that a DTM does not include vegetation (Figure 6). To successfully produce a DTM, AggieAir technicians used Agisoft to isolate and remove vegetation through altering variables that define maximum allowable slope and cell size. Once removed, the new DTM underwent smoothing to fill holes left behind from the deletion of cells that were found to represent vegetation elevation rather than surface elevation. This step produced a DTM, also at a resolution of 2.3 cm per pixel (Figure 4, Table 2). In addition to the data outlined above, data for Polygon 2 also consisted of uncalibrated (meaning there was no external thermal ground-truthing data collected) thermal mosaics with data in degrees Celsius and a resolution of about 15 cm per pixel (Figures 4 and 5, Table 2).

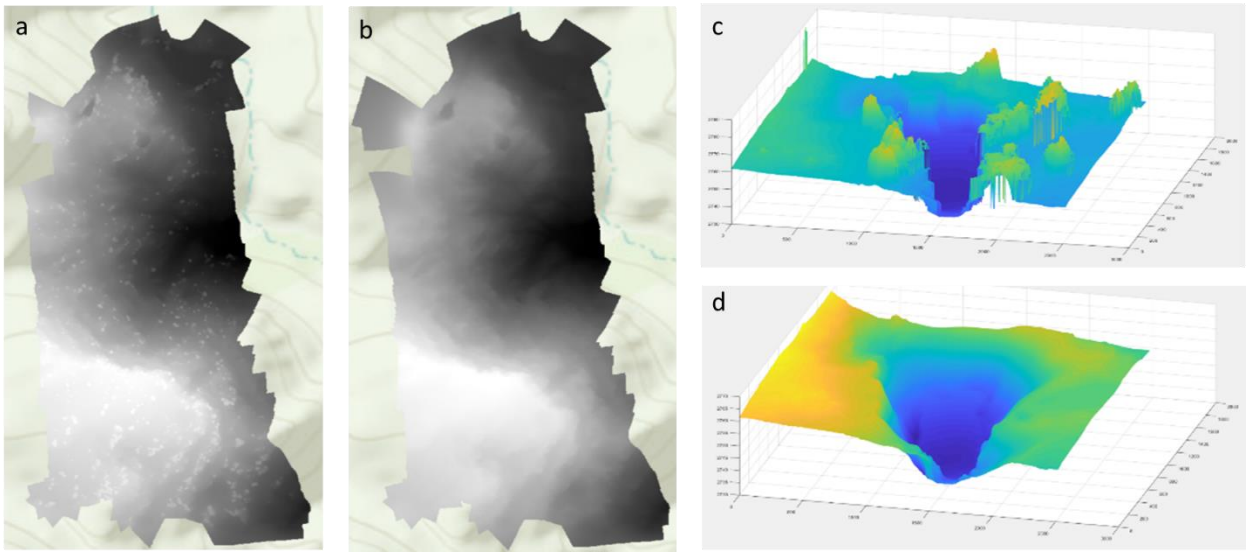

Figure 6: Polygon 2 DSM (includes vegetation) (a) and DTM (vegetation removed) (b). Area in Polygon 2 clipped to a known large karst feature (c, d). Clipped DSM (includes vegetation) (c) and clipped DTM (vegetation removed) (d). Vegetation removal processed by AggieAir Technician through Agisoft Software.

In some of the analyses outlined below, attempts at processing the whole study area using MATLAB failed due to available processing power and the large file size. Therefore, three small areas were clipped from Polygon 2 for each of the uncalibrated thermal mosaics, the 4-band reflectance mosaics, and the DTM rasters (Table 2). These clipped locations were limited to three areas that contained known surficial karst features at three different scales (Figure 7). From this point on, those clipped locations will be referred to as the large karst feature (Figure 4b), the medium karst feature (Figure 4c), and the small karst feature (Figure 4d). The large karst feature has an opening on the scale of approximately 30m x 10m. The medium karst feature has an opening at a scale around 25m x 10m. The small karst feature has an opening of approximately 3m x 2m.

Table 2: Outline of the data used in the analysis of this study. Contains remotely sensed data products and their resolution and source.

Remotely Sensed Data	**Resolution**	**Source**
Red Green Blue Spectral Imagery	3 – 5 m	Planet's Satellite Data
Near-Infrared RapidEye Analytic Ortho Tile Data	3 – 5 m	Planet's Satellite Data
4-Band Reflectance Mosaics	0.023 m	UAV Flight
Digital Surface Model (DSM)	0.023 m	UAV Flight
Digital Terrain Model (DTM)	0.023 m	Digital Surface Model
Uncalibrated Thermal Mosaics	0.15 m	UAV Flight

Clipped 4-Band Reflectance Mosaics (Clipped to the location of Large, Medium, and Small Karst)	0.023 m	UAV 4-Band Reflectance Mosaics
Clipped Digital Terrain Model (Clipped to the location of Large, Medium, and Small Karst)	0.023 m	Digital Terrain Model
Clipped Uncalibrated Thermal Mosaics (Clipped to the location of Large, Medium, and Small Karst)	0.15 m	Uncalibrated Thermal Mosaics

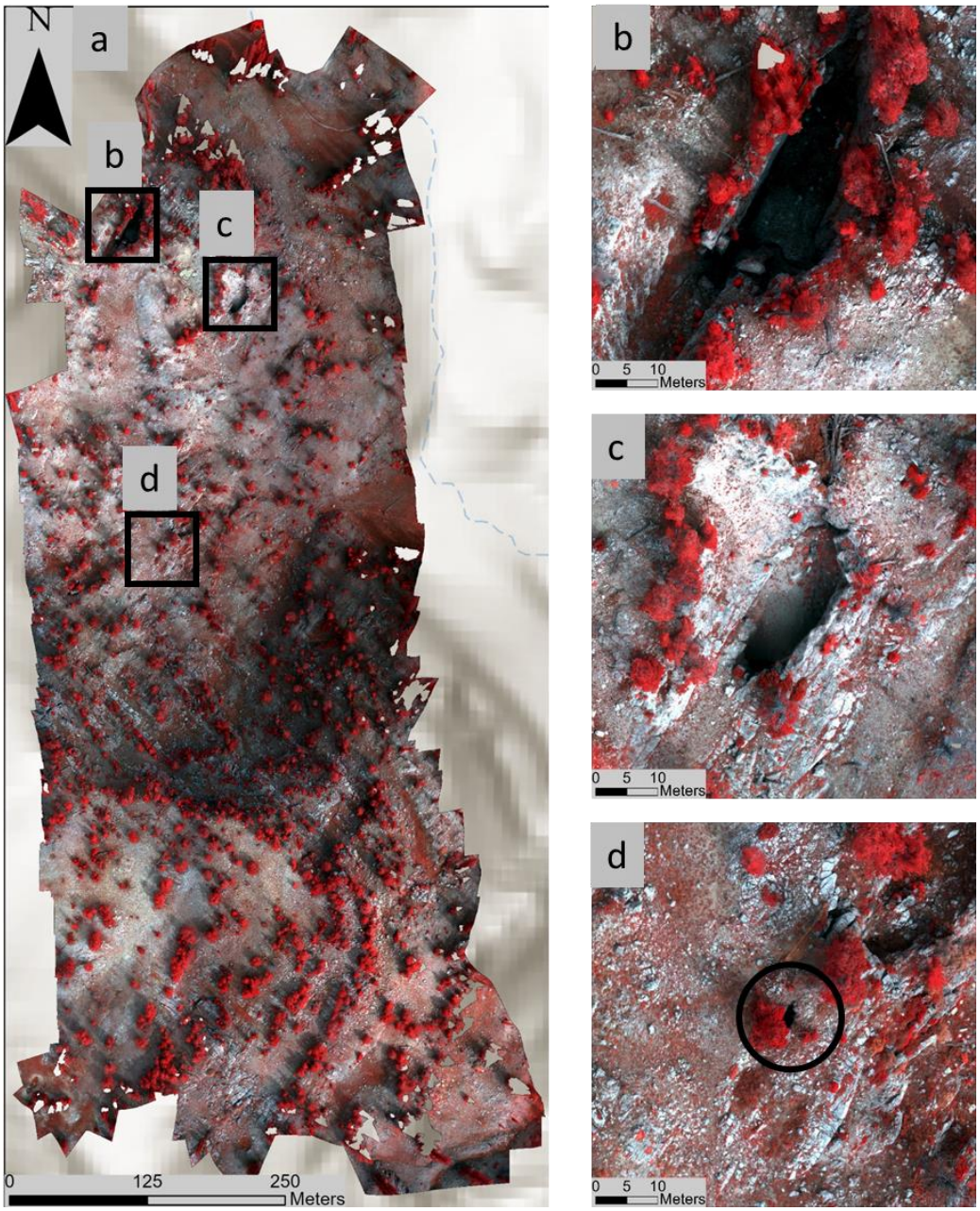

Figure 7: False-color composite of Polygon 2 (a) and clipped areas within (b – d) limited to large (b), medium (c), and small (d) karst features.

Data Analysis

The first set of analyses for this study investigated different data products and spatial resolutions to understand the level of detail needed to identify unique signatures associated with surficial karst features. Visual methods of identifying karst signatures began with Planet's satellite data at a resolution of 3 – 5 meters per pixel (Table 3). To begin, nearby temperature and relative humidity (RH) data were collected for 2016 through 2017 from a local Logan River Observatory weather station (Tony Grove Climate Station) (LRO, 2021). Based on that data, it was determined that February 2016 and August 2017 had the most significant difference between temperature and RH. This led to Planet's RGB-NIR satellite data being downloaded for those months. Then, ArcMap software was used to create a Normalized Difference Vegetation Index (NDVI) layer (Eqn. 1), a false-color composite layer, and a Near-Infrared (NIR) layer (Table 3).

$$NDVI = \frac{NIR-R}{NIR+R} \quad \text{Eqn. 1}$$

where

NIR = Near-Infrared Band

R = Red Band

The NDVI layer displays calculated reflectance properties based on the difference between NIR and red wavelength reflectance. This method returns values ranging from 0 to 1, where values close to 0 represent barren areas and values close to 1 represent high reflectance vegetation. To perform the NDVI calculations, the Band Arithmetic function in ArcGIS Pro was used. While there are many types of vegetation indices that can be calculated, the NDVI was initially used because it is the most common vegetation index for identifying vegetation (Gao, 1996). Using the NDVI layers, false-color composite

layers, and NIR layers, a visual comparison between months was completed in an attempt to identify anomalies in the location of known karst features.

The second analysis was the first to use the UAV collected data for Polygon 2 (Table 3). It focused on limiting the search area for karst features by eliminating locations where surficial karst was not present or could not be detected. First, an analysis of the spectral layers was completed (Table 3). Due to the nature of the UAV data and the cameras' inability to penetrate dense vegetation, no analysis of the terrain shrouded by vegetation could be completed (Wallace et al., 2016). Therefore, the first layer was created by simply removing vegetation based on sampled reflectance values. This was completed by creating a vegetation index and then sampling the reflectance of vegetation within Polygon 2 to obtain a representative range of values. That range of reflectance values was then used to filter the vegetation index layer and remove these data.

NDVI was initially used in this analysis. However, after sampling reflectance properties within the study area, it was found that highly reflective carbonate in the area created an overlap in vegetation and bedrock reflectance values. Therefore, the vegetation index that was ultimately applied was the Soil Adjusted Vegetation Index (SAVI) using Eqn. 2.

$$SAVI = \left(\frac{NIR-R}{NIR+R+L}\right) * (1+L) \qquad \text{Eqn. 2}$$

where

NIR = Near Infrared Band

R = Red Band

L = Soil Correction Factor (L = 0.5)

Similar to NDVI, SAVI returns reflectance values that range from 0 to 1. This vegetation index is preferable in this instance because it applies a soil correction factor (L), which results in a more significant difference between values obtained from the highly reflective carbonate bedrock and vegetation. This layer was also created in ArcMap using the Band Arithmetic function.

A shapefile consisting of points at locations with vegetation was created for identifying a range of reflectance values for vegetation within the study area. ArcMap's Extract Multiple Values to Points tool was then used to pull SAVI values at those locations and add them to the shapefile's attribute table. The minimum and maximum values were identified and used in ArcMap's Set to Null tool. This tool ultimately masked, or removed, all data that included reflectance values within the defined range from the SAVI layer. Additionally, because the desire is only to retain locations where the surficial karst features could be detected, once the SAVI layer had the undesirable data removed, it was used to clip corresponding data from the DSM.

A similar methodology as outlined above for the spectral analysis was used to mask thermal data (Table 3). Though the first hundred meters of karst systems are influenced by external temperatures and seasonal variations, the temperature at the openings is also a function of radiation, precipitation, evapocondensation, and thermal exchanges between soil and air (Luetscher and Jeannin, 2004). Preliminary results also showed a difference in temperature among the karst openings and the surrounding areas between the hours that the UAV flight was conducted (Figure 8). Therefore, proceeding with that understanding, thermal values for known karst feature locations were sampled to create a range of temperatures. Those temperatures were presumed to be representative of karst features within the study area and used to mask temperatures outside of that range. The resulting SAVI and thermal layers were then combined to create a new layer that only included data common to both datasets (Table 3).

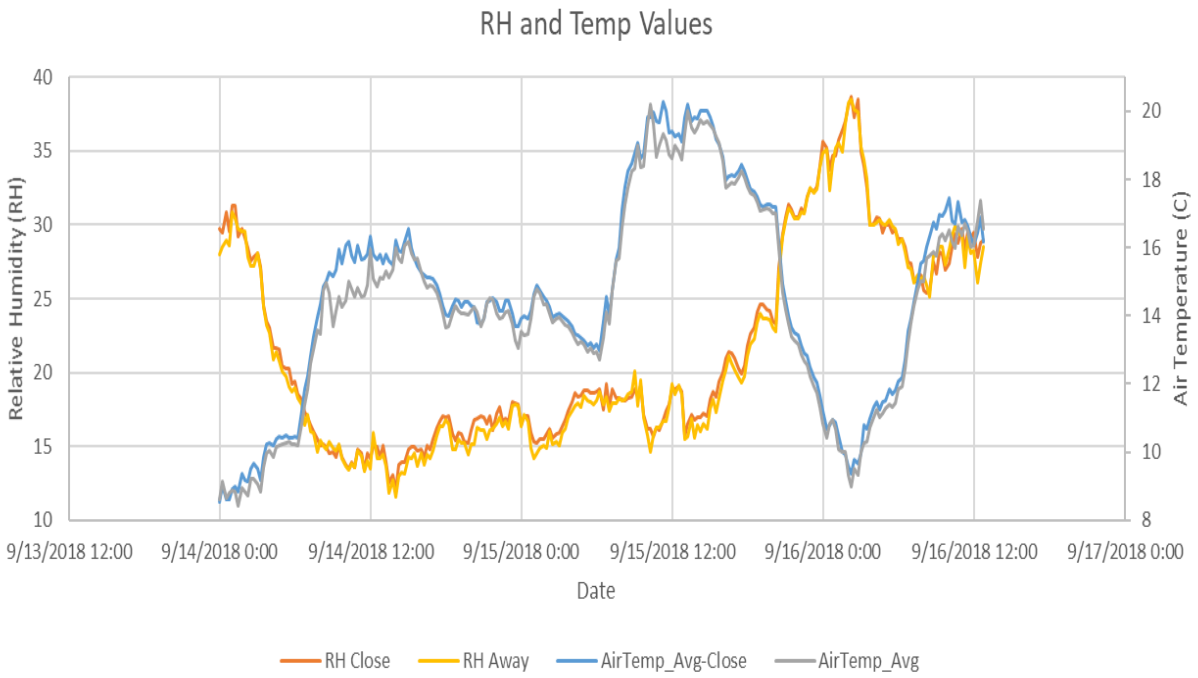

Figure 8: Preliminary data collected by deploying two temperature and RH sensors. One sensor was placed close to a karst opening (RH Close and AirTemp_Avg Close), and a second placed ~10 m away from the karst opening (RH Away and Air Temp_Avg).

The third data analysis approach focused on using edge detection to identify karst feature signatures. Using the 2.3 cm per pixel DTM for the large, medium, and small karst subsections of Polygon 2, edge detection methods were applied to the raw, smoothed, and differenced data (Table 3). Smoothing is commonly used to reduce noise within an image (Weickert, 1998). For this study, smoothing was tested using two different methods. The first method of smoothing is a moving average. This method defines the size of matrices and then calculates an average around a center pixel. The user can define the size of the matrix as well as the number of iterations performed. Various values were tested for both the size of the matrix and the number of iterations used.

The second method of smoothing is Gaussian smoothing (Table 3). Through this smoothing method, the user can define the value of sigma (σ), where σ is the standard deviation of the Gaussian distribution and a larger σ results in increased "blurring." This smoothing method was applied using an array of different σ values to complete isotropic smoothing of the clipped DTMs. Utilizing the outputs

from the smoothing processes, the images were differenced. To complete this process, the elevations contained within the smoothed DTMs were subtracted from the original elevations contained within the clipped DTMs to create the new differenced elevation model.

Edge detection is used to determine where the edges of features may exist. This study used three edge detection methods: the Canny, Sobel, and Roberts edge detection methods (Table 3). All three methods were used on the raw DTMs, the smoothed DTMs, and the DTMs obtained from image differencing. The various methods of edge detection were used to locate enclosed circular edges. The Canny edge detection method works by identifying local maxima in the gradient, calculated as the derivative of a Gaussian filter. Canny utilizes strong and weak edges, but only includes weak edges if connected to strong edges (Gonzalez et al., 2009). Sobel edge detection locates edges by computing the gradient through calculating differences in rows and columns in a 3 x 3 neighborhood. Additionally, the center pixel is weighted by 2 to provide smoothing (Gonzalez et al., 2009). Roberts edge detection is one of the oldest and simplest edge detection methods in digital image processing. It detects edges by approximating first derivatives as differences between adjacent pixels (Gonzalez et al., 2009).

Curvature calculations were completed on the small, medium, and large clipped subsections of Polygon 2 at the original resolution (Table 3). Prior to calculating curvature, smoothing by the Weickert method was performed to reduce noise in the image and still preserve regional edges through implicit discretization. This method of smoothing utilizes the COHERENCEFILTER function to perform anisotropic diffusion in 2 dimensions. The parameters T (the total diffusion time) and dt (the diffusion time step) were adjusted in the process. These parameters define the number of coherence filter iterations. Simple 2-D curvature calculations were then completed. Once curvature was shown to be a potentially useful method for identifying a signature of karst features, the resolution of the data clipped from Polygon 2 was coarsened. This was completed to test the resolution of data needed to identify the curvature of

the karst openings. The data representing the small, medium, and large karst features were aggregated through bilinear interpolation to a range of resolutions, noted in Table 3. Based on the findings from calculating the curvature of clipped data at various resolutions, the whole of Polygon 2 was similarly aggregated using bilinear interpolation to resolutions of 0.1, 0.5, and 1-meter per pixel to test and visualize the results of calculating curvature at different spatial scales (Table 3). Using methods already outlined, the Weickert method of smoothing and curvature calculations were performed on the aggregated data of Polygon 2.

To determine if topography alone could be used to identify sinkholes, watershed delineation was performed on the unclipped Polygon 2 study area using the 1-meter resolution and identified sinks as pour points. Various neighborhoods, defined by the size and shape of a matrix, were used to run focal statistics properties in ArcGIS (Table 3). The neighborhoods and defined variables used to run focal statistics for each can be seen in Table 3. Flow Direction was then calculated for each of the resulting layers. Then using the Sink tool in ArcMap, a layer was created showing locations which had been identified as sinks. Watershed delineation then followed by using the sink locations as pour points. These delineated watersheds helped detect locations identified as sinks, which were as small as a single pixel in some cases. Finally, the results from calculating curvature, locating sinks, and performing watershed delineations were overlayed on each other (Table 3). This was completed to add supporting evidence or refute predictions of locations of karst features.

Table 3: Outline of data analysis performed. Includes data created, location of geo-located data, data used to perform analysis, and the resolution of the data produced.

Analysis	Data Created	Location	Data Used	Resolution
1	Normalized Difference Vegetation Index	Tony Grove Study Area	Planet's Satellite Data	3 – 5 m
	False Color Composite	Tony Grove Study Area	Planet's Satellite Data	3 – 5 m
	Near-Infrared Display	Tony Grove Study Area	Planet's Satellite Data	3 – 5 m
2	Spectral Analysis	Polygon 2	UAV 4-Band Reflectance Mosaics	0.023 m
	Thermal Analysis	Polygon 2	UAV Uncalibrated Thermal Mosaics	0.15 m
	Spectral and Thermal Compilation	Polygon 2	Results of Spectral and Thermal Analysis	0.023 m and 0.15 m
3	Moving Average Smoothing	Large, Medium, and Small Karst Clips	Clipped Digital Terrain Model	0.023 m
	Gaussian Smoothing	Large, Medium, and Small Karst Clips	Clipped Digital Terrain Model	0.023 m
	Image Differencing with Moving Average Smoothing	Large, Medium, and Small Karst Clips	Clipped Digital Terrain Model - Moving Average Smoothing	0.023 m
	Image Differencing with Gaussian Smoothing	Large, Medium, and Small Karst Clips	Clipped Digital Terrain Model - Gaussian Smoothing	0.023 m
	Canny Edge Detection	Large, Medium, and Small Karst Clips	Clipped Digital Terrain Model	0.023 m
			Moving Average Smoothing	0.023 m
			Gaussian Smoothing	0.023 m
			Image Differencing with Moving Average Smoothing	0.023 m
			Image Differencing with Gaussian Smoothing	0.023 m
	Sobel Edge Detection	Large, Medium, and Small Karst Clips	Clipped Digital Terrain Model	0.023 m
			Moving Average Smoothing	0.023 m
			Gaussian Smoothing	0.023 m

Analysis	Data Created	Location	Data Used	Resolution
			Image Differencing with Moving Average Smoothing	0.023 m
			Image Differencing with Gaussian Smoothing	0.023 m
	Roberts Edge Detection	Large, Medium, and Small Karst Clips	Clipped Digital Terrain Model	0.023 m
			Moving Average Smoothing	0.023 m
			Gaussian Smoothing	0.023 m
			Image Differencing with Moving Average Smoothing	0.023 m
			Image Differencing with Gaussian Smoothing	0.023 m
4	Aggregated Clipped Digital Terrain Model	Large, Medium, and Small Karst Clips	Clipped Digital Terrain Model	0.05 m
				0.075 m
				0.1 m
				0.25 m
				0.5 m
				0.75 m
				1 m
				2.5 m
				5 m
				7.5 m
				10 m
	Weickert Smoothing	Large, Medium, and Small Karst Clips	Clipped and Aggregated DTMs	0.023 – 10 m
	2-D Curvature	Large, Medium, and Small Karst Clips	Clipped and Aggregated DTMs	0.023 – 10 m
	Aggregated Digital Terrain Model	Polygon 2	Digital Terrain Model	0.1 m
				0.5 m
				1 m

Analysis	Data Created	Location	Data Used	Resolution
	Weickert Smoothing	Polygon 2	Aggregated Digital Terrain Models	0.1 – 1 m
	2-D Curvature	Polygon 2	Aggregated Digital Terrain Models	0.1 – 1 m
5	Focal Statistics, Neighborhood: Rectangular 3 x 3, Statistic Type: Minimum	Polygon 2	Digital Terrain Model	1 m
	Focal Statistics, Neighborhood: Rectangular 3 x 3, Statistic Type: Mean			
	Focal Statistics, Neighborhood: Rectangular 5 x 5, Statistic Type: Minimum			
	Focal Statistics, Neighborhood: Rectangular 5 x 5, Statistic Type: Mean			
	Focal Statistics, Neighborhood: Circular w/ Radius of 3, Statistic Type: Mean			
	Focal Statistics, Neighborhood: Annulus w/ Inner Radius of 1 and Outer Radius of 3, Statistic Type: Mean			
	Focal Statistics; Neighborhood: Wedge w/ Radius of 3, Start Angle of 0, and End Angle of 90; Statistic Type: Mean			
	Focal Statistics, Neighborhood: Irregular 3 x 3, Statistic Type: Mean			
	Focal Statistics, Neighborhood: Weight 3 x 3, Statistic Type: Mean			
	Flow Direction	Polygon 2	Focal Statistics Results	1 m
	Sink Identification	Polygon 2	Flow Direction	1 m
	Watershed Delineation	Polygon 2	Flow Direction and Sink Identification	1 m
6	Curvature and Watershed Compilation	Polygon 2	2D Curvature, Sink Identification, Watershed Delineation	1 m

Results

The first analysis performed tested Planet's high-resolution satellite imagery to determine if the resolution of data required to identify signatures unique to surficial karst features already existed for the defined study area. Data for the large karst feature location show anomalies occurring around the location of this known karst features and between times of the year with differing temperatures and RH (Figure 9 b – g). Through visually inspecting the false-color composite layer (Figure 9 b – c), the NDVI layer (Figure 9 d – e), and the NIR layer (Figure 9 f – g), it is apparent that there are differences between the known locations of karst features and the surrounding areas. Differences are also visible in the same locations, but at different times of low and high temperatures and relative humidity (Figure 9). However, the resolution of the data makes it difficult to have confidence in karst feature locations. It was determined that data at the resolution of 3 – 5 meters per pixel is not fine enough to test various methodologies for identifying karst signatures.

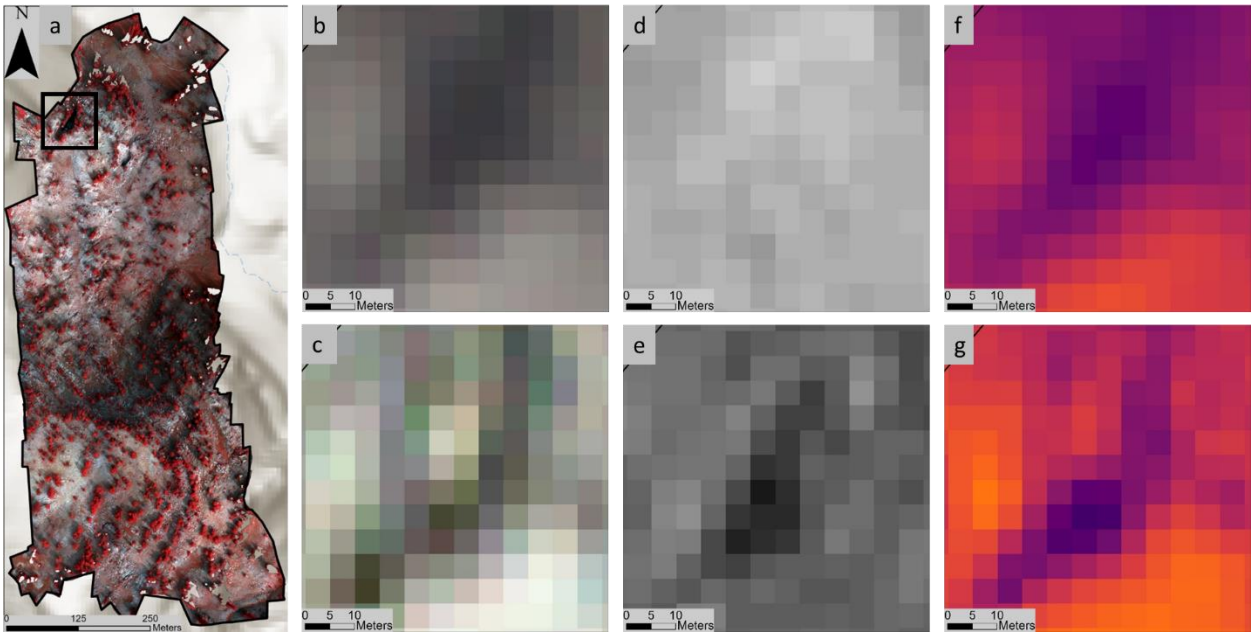

Figure 9: Results obtained from Planet's 3 – 5 meter resolution satellite imagery. Figure 9a displays a false-color composite of Polygon 2 using much finer UAV data. Figures b, d, and f displays data collected during a period of low temperature and relative humidity (February 2016), and c, e, and g displays data collected during high temperature and relative humidity (August 2017). Figures 9 b – g display the results obtained by using Planet data in the known location of a large karst feature using false-color composite (b, c), NDVI (d, e), and near-infrared (f, g) layers.

Initial analysis of UAV imagery consisted of limiting data to locations where karst features could exist and be detected, based on a range of sampled values from the SAVI and thermal rasters. As discussed in the methods, values found to be outside of an acceptable selection for the corresponding data layers were removed to create filtered datasets. Spectral analysis using SAVI successfully eliminated areas where karst features could not be detected (Figures 10 and 11). Due to processing methods and the nature of the collected data, locations of karst shrouded by vegetation were unobservable. The results from a Soil Adjusted Vegetation Index and a Normalized Difference Vegetation Index were compared to each other, as well as to a false-color composite, for Polygon 2 (Figure 10 a – c). Results from calculating the NDVI layer provided reflectance values ranging from 0 – 0.90 (Figure 10b). Sampling vegetation within the NDVI layer resulted in a range of values from 0.59 – 0.9. Values within the NDVI layer for Polygon 2 within that range were then removed. Similarly, SAVI results produced reflectance values ranging from 0 – 0.72 (Figure 10c). Sampling vegetation using the SAVI layer (Figure 11) resulted in a range of values between 0.27 – 0.72. Again, using the resulting range of values, the SAVI layer of Polygon 2 with values within the range were filtered out. It was found that even though NDVI and SAVI both underwent similar methods of sampling vegetation and filtering values out, SAVI was more successful at distinguishing between the reflectance of vegetation and the highly reflective bedrock in the area (Figure 11).

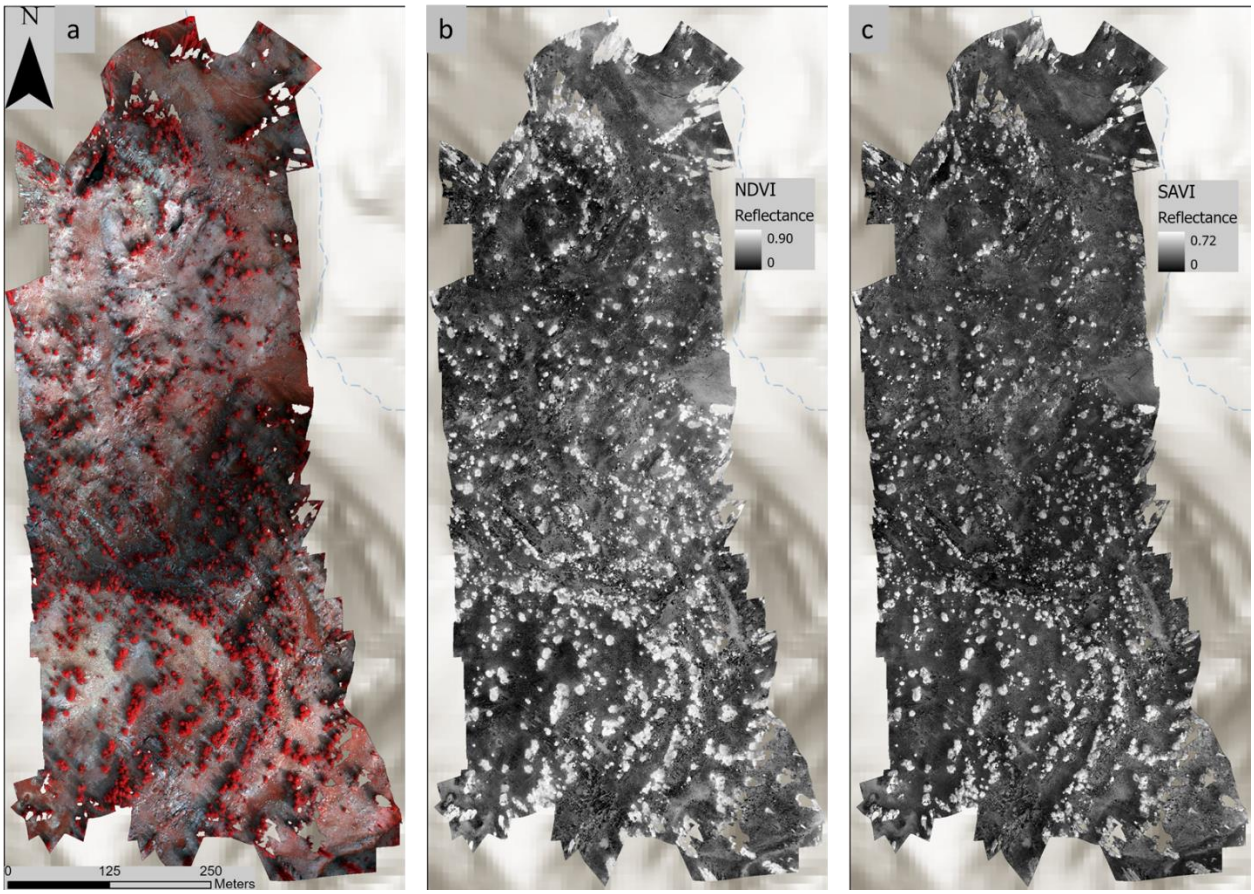

Figure 10: Reflectance values and contrast between vegetation and the surface obtained by using NDVI and SAVI indexes. False-color composite (a), results of NDVI (b), results of SAVI (c).

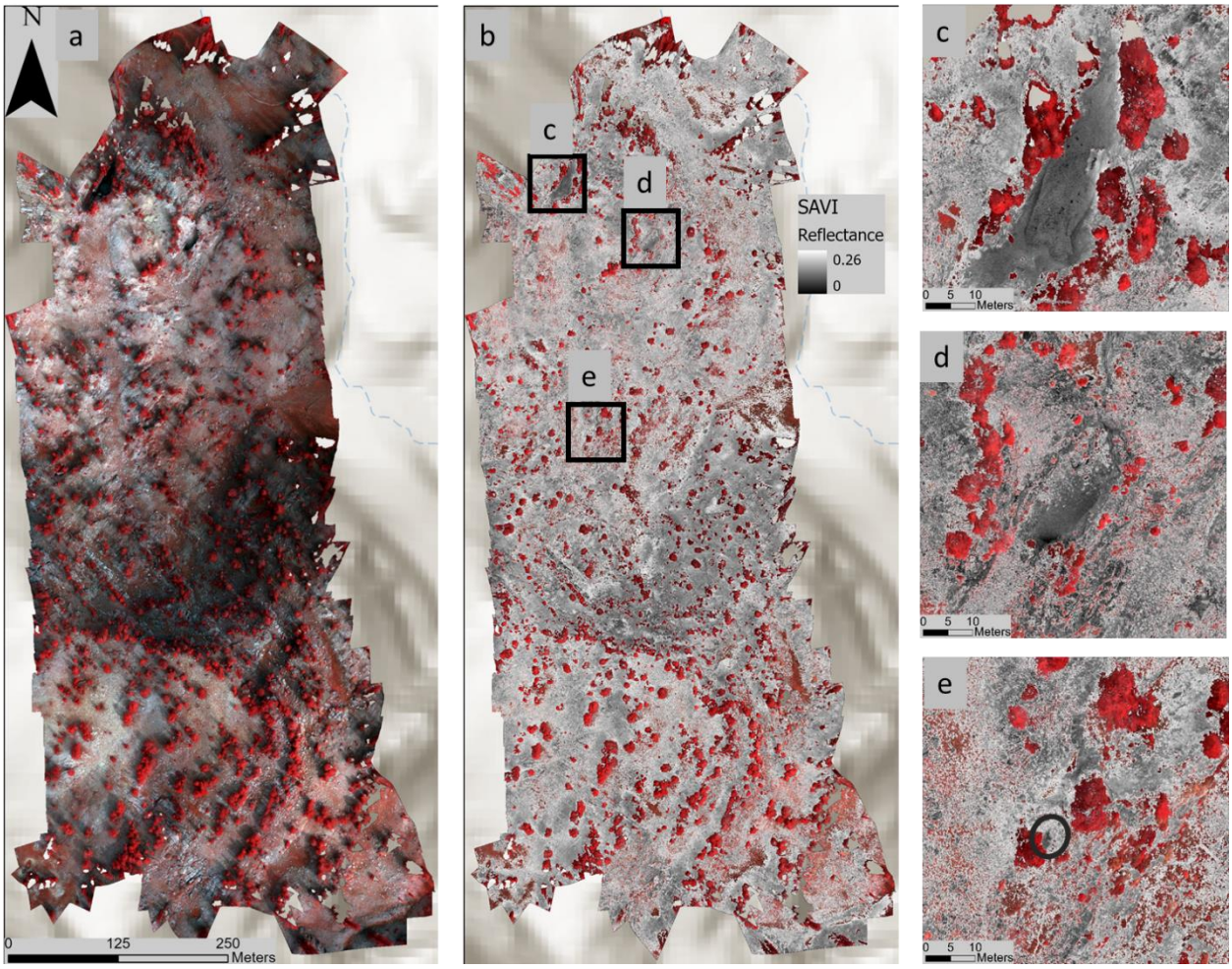

Figure 11: Filtered reflectance values. False-color composite (a), filtered SAVI layer overlaying a false-color composite layer (b), large karst location (c), medium karst location (d), small karst location (e).

The thermal analysis was completed using a similar process to that of the spectral analysis, that is by limiting temperatures within the thermal dataset based on known sinkhole locations. While it was expected that large swaths of data would be removed, it was found to only be successful in locations that were exposed to sunlight. Still, in those sunny locations, this method was much more successful than SAVI (Figure 12). Unfortunately, shaded areas had thermal signatures within the range of temperatures sampled from known karst features, resulting in less data removal than sunlit areas. In the end, the thermal analysis proved to be very useful in limiting search areas for locations that were exposed to sunlight and that were not shrouded by vegetation (Figure 12). As such, this method was found to be only partially successful at identifying karst feature locations.

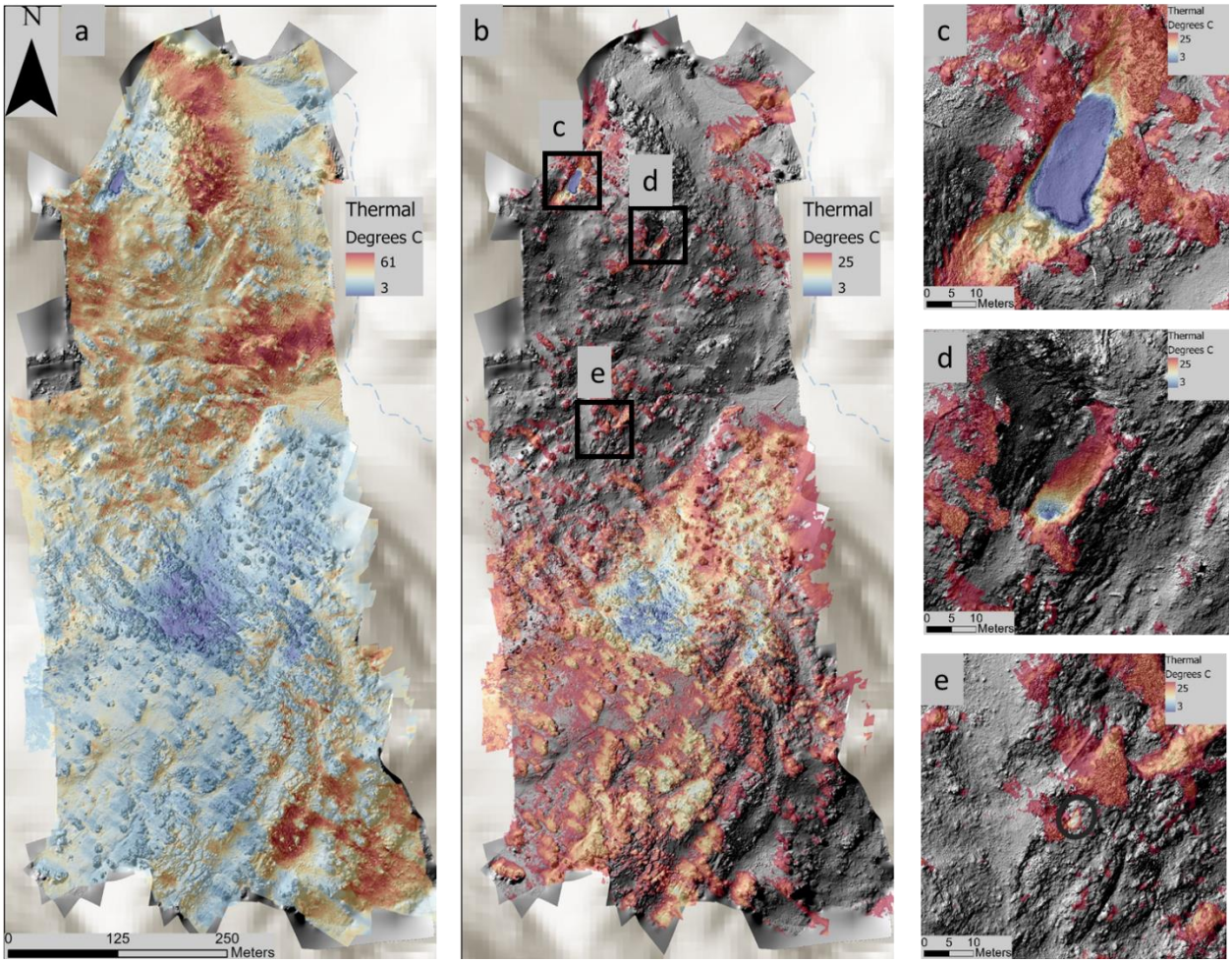

Figure 12: Results of filtering using thermal imagery. An unaltered thermal layer (a), filtered thermal layer on a hillshade (b), large karst location (c), medium karst location (d), small karst location (e).

Given that both the thermal and spectral analysis were only partially successful and each method had different weaknesses, the combination of these results were combined to create more evidence regarding potential karst feature locations (Figure 13). By combining the SAVI and thermal layers, the area was further reduced, however, the potential karst locations included a large portion of the study area.

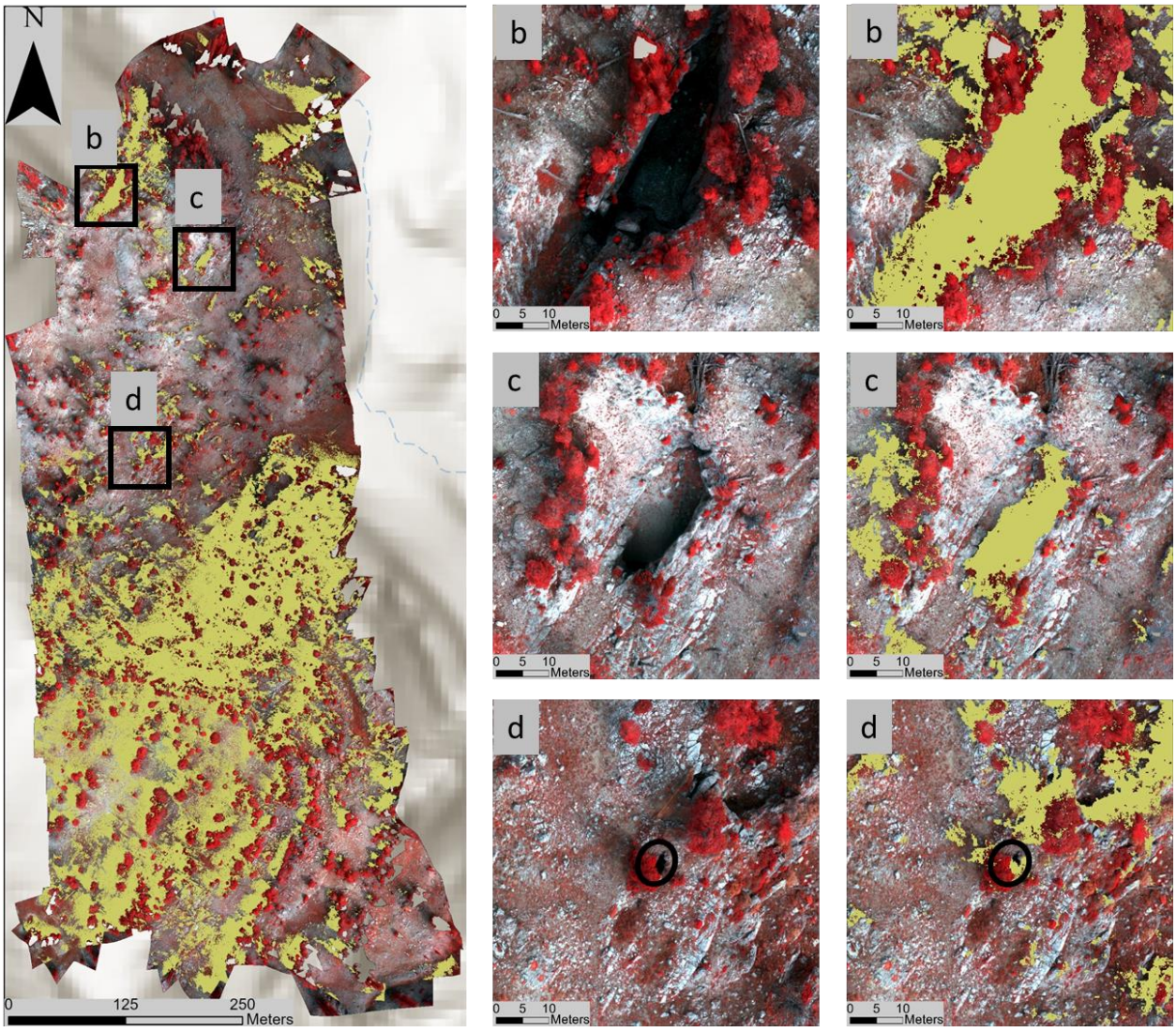

Figure 13: Results of limiting layers to include areas that meet all constraints from masking SAVI and thermal (a) with small (d), medium (c), and large (b) karst features blown up.

It was anticipated that karst features could be identified by their edges. Therefore, in continuing the search for methods that could successfully provide a unique surficial karst signature, multiple edge detection methods were explored. While these edge detection methods were used on DTM's directly, they were also used on smoothed DTMs and differenced DTMs. Smoothing was completed to reduce noise when used with edge detection methods and enhance edge features when used with image differencing. The new layers were created from moving average and Gaussian smoothing methods (Figures 14 and 15). When comparing the data from the original DTM (Figure 14a) to increasingly

smoothed topography (Figures 14b – d), it is clear that an increased matrix size used to calculate the average value at the center pixel results in increased smoothing.

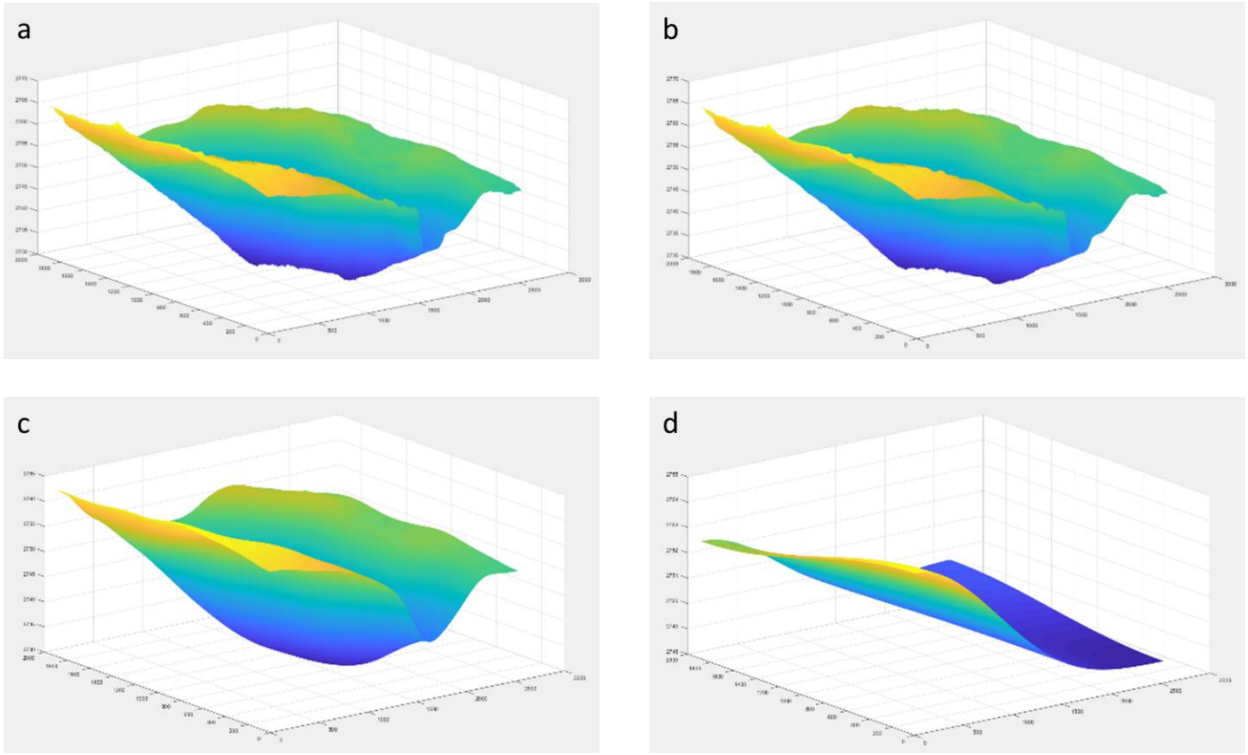

Figure 14: Original DTM with 2.3 cm resolution limited to the large karst feature area (a). Moving average smoothing performed on large karst feature (b – d). 3 x 3 Matrix with 10 iterations (b), 100 x 100 Matrix with 10 iterations (c), 1000 x 1000 Matrix with 10 iterations (d).

Similarly, the topography in the original 2.3 cm resolution DTM clipped to the large karst feature location (Figure 15a) was smoothed using the Gaussian method where σ is increased (Figure 15b – d). It can be seen that as σ increased, the topography again becomes increasingly smoother. Both methods offered a noise reduction, but also resulted in the smoothing of the identified karst features. Though there were differences in the results of using the moving average method versus the Gaussian method of smoothing, it was not immediately apparent which smoothing method provided a more desirable result.

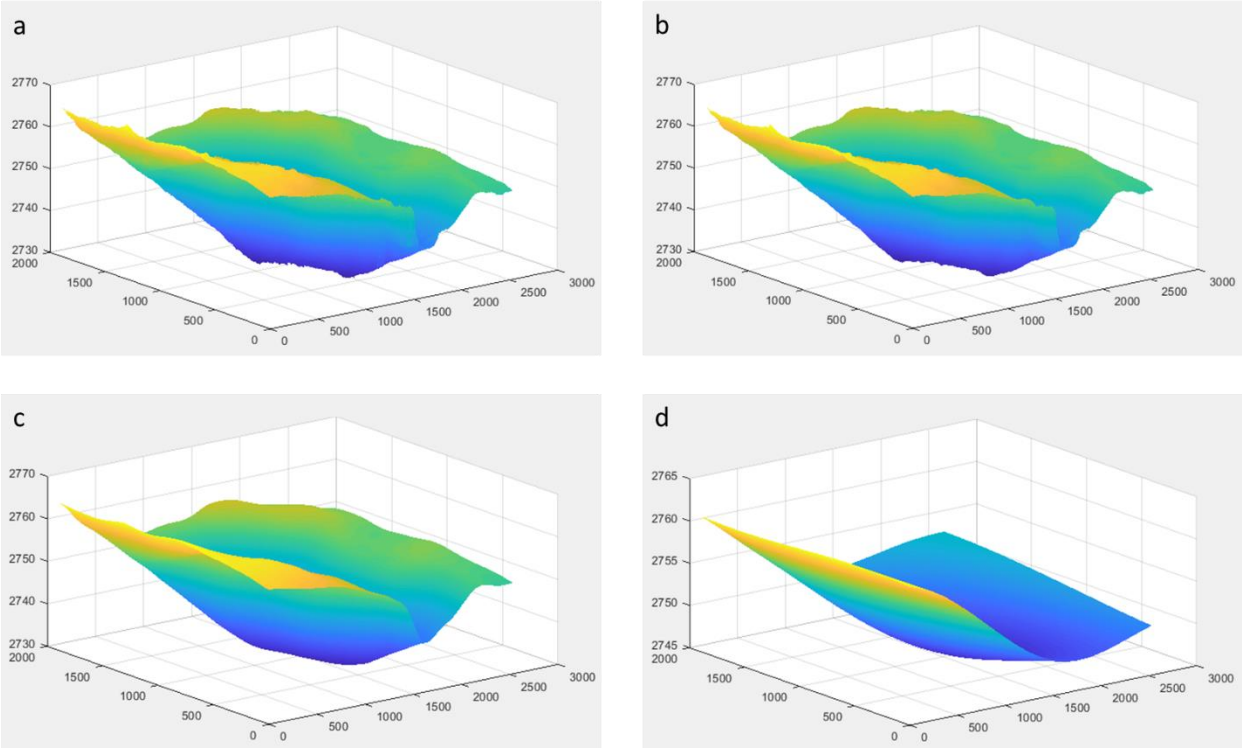

Figure 15: Original DTM with 2.3 cm resolution limited to the area of the large karst feature (a). Gaussian smoothing performed on large karst feature (b – d), σ = 6 (b), σ = 60 (c), σ = 600 (d).

Image differencing, or the differencing of a smoothed DTM from the original DTM, was the first method that directly made use of the smoothed DTM layers (Figure 16). Figure 16a was created by subtracting the layer produced by using the moving average filter with a matrix of 100 x 100 with 10 iterations (Figure 14c) from the original DTM limited to the area of a large karst feature (Figure 14a). Similarly, Figure 16b was obtained by subtracting the layer produced by using the Gaussian Filter with σ = 60 (Figure 15c) from the original DTM limited to the area of a large karst feature (Figure 15a). Image differencing resulted in edges of the large karst feature being enhanced in some locations around the opening. However, because the enhanced edge around the karst feature is not consistent, it does not produce the desired result of a continuous encompassing boundary. Again, it is not apparent which method of smoothing produced a more desirable result.

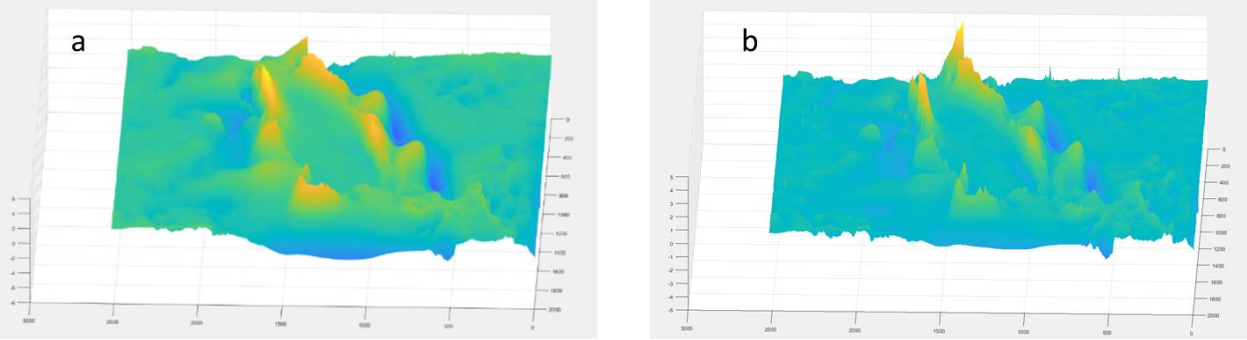

Figure 16: Results of image differencing layers with a 2.3 cm resolution where (a) is obtained from subtracting the layer produced by using the moving average filter with a matrix of 100 x 100 with 10 iterations (Figure 14c) from the original DTM limited to the area of a large karst feature (Figure 14a). (b) is obtained by subtracting the layer produced by using the Gaussian filter with σ = 60 (Figure 15c) from the original DTM limited to the area of a large karst feature (Figure 15a).

The desired outcome of edge detection methods was to identify a continuous edge that encircled an area around the locations of known surficial karst features. The results of using the Canny edge detection method with smoothed data layers showed some promise (Figure 17). Figure 17a – c was obtained from using Canny edge detection with the moving average method of smoothing with 20 (a), 25 (b), and 30 (c) iterations of a 10 x 10 matrix. Figure 17d – f shows the results from using Canny edge detection with the Gaussian smoothing method where the values of σ = 14 (d), 16 (e), and 18 (f). It was found that using Canny edge detection on the data layer produced from the Gaussian smoothing method with σ = 16 provided the closest figure to the desired result (Figure 17e). Through visibly comparing results, Canny edge detection appeared more successful at removing undesirable noise and producing a more continuous boundary around the known karst features than both the Sobel and Roberts edge detection methods. Even with Canny's ability to detect strong and weak edges, it failed to provide a continuous edge around the known karst features.

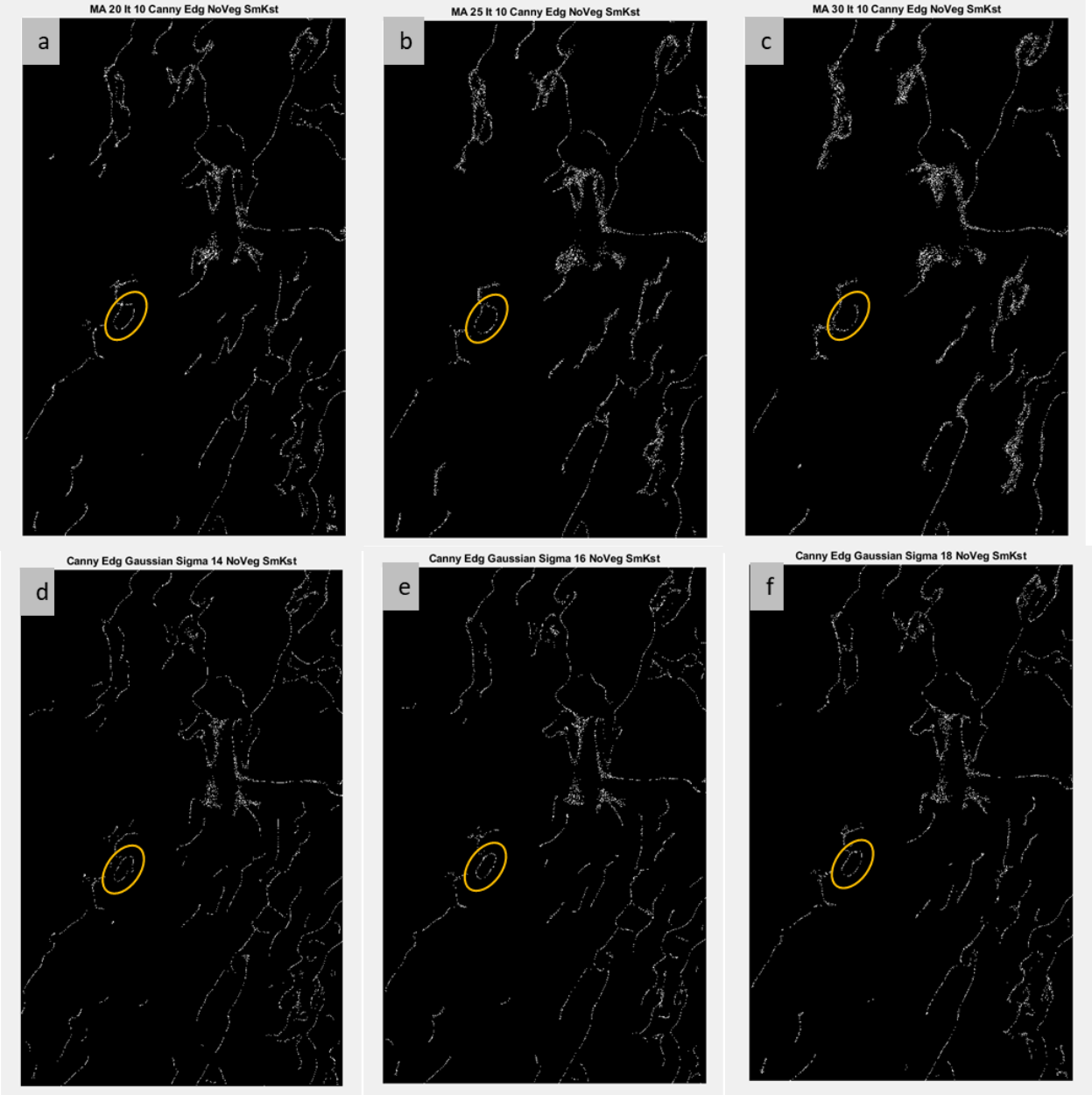

Figure 17: Comparing Canny edge detection method used with moving average filter (a – c) and Canny edge detection method used with Gaussian smoothing filter (d – f). The top three images show Canny edge detection used with moving average smoothing with a 10 x 10 matrix with 20 iterations (a), 25 iterations (b), and 30 iterations (c). The bottom three images show the results of using the Canny edge detection method used with Gaussian smoothing when σ = 14 (d), σ = 16 (e), and σ = 18 (f).

Curvature calculations were looked at as a method to produce results with a more complete boundary around known karst features. First, utilizing clipped locations within Polygon 2 at the original 2.3 cm resolution, curvature calculations were expected to result in concentric rings of positive curvature around known sinkholes. Results of curvature calculations were promising on the small, medium, and large karst features at the very high 2.3 cm resolution (Figure 18a); however, as clipped

data was aggregated to more coarse resolutions, findings changed (Figure 18 b – l). Curvature calculations on aggregated data showed that even with the largest karst feature in Polygon 2, 2.5 m pixel resolution became too coarse (Figure 18i). Conversely, Figure 18 a – e, shows that when the resolution is too fine, undesirable noise increased, making it harder to identify/isolate the desired signatures. It was found that resolutions between 0.5 and 2.5 meters per pixel sufficiently produced the desired signature while reducing undesirable noise (Figure f – h). It was determined that processing requirements to calculate curvature for the whole of Polygon 2 would be met if the resolution of data were aggregated to the 1-meter resolution.

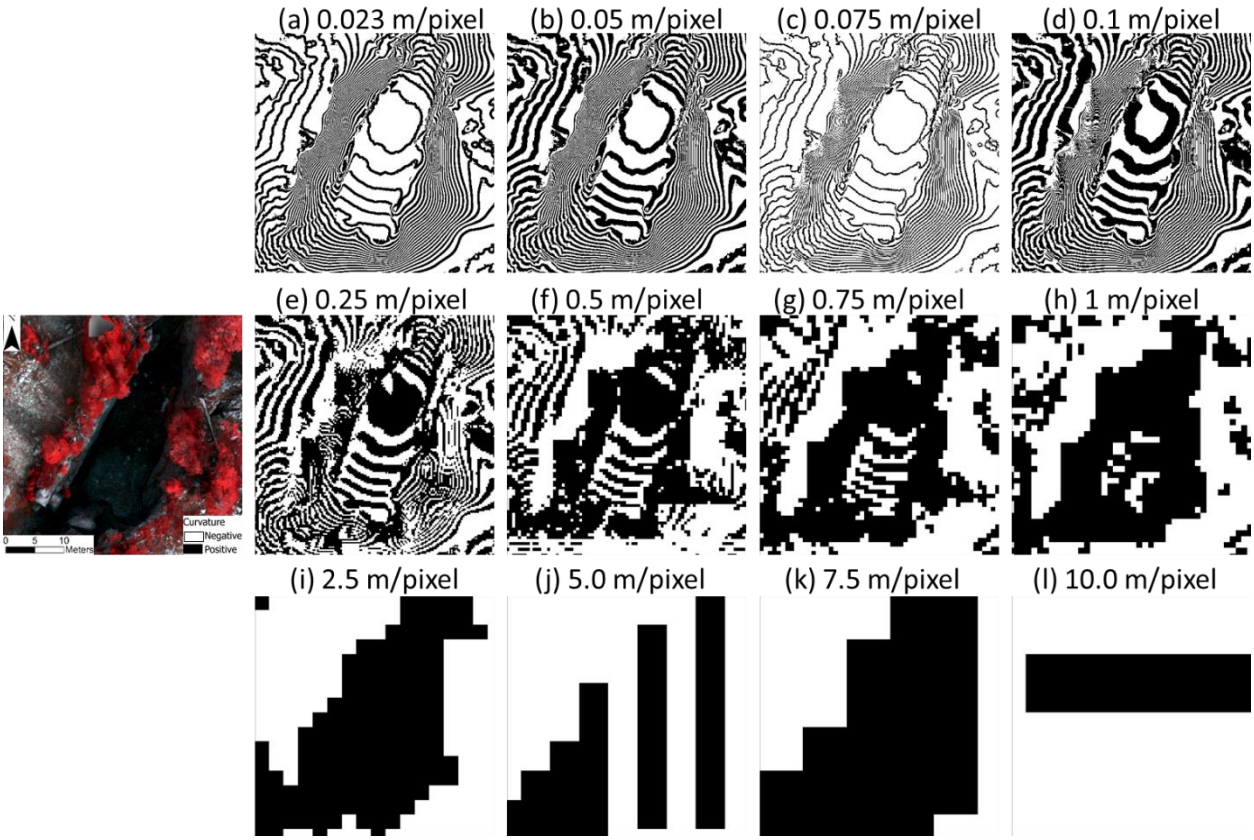

Figure 18: RGB data clipped to area of a known large karst feature (left), compared to curvature calculated at various aggregated resolutions, where resolution specific to each image is noted above.

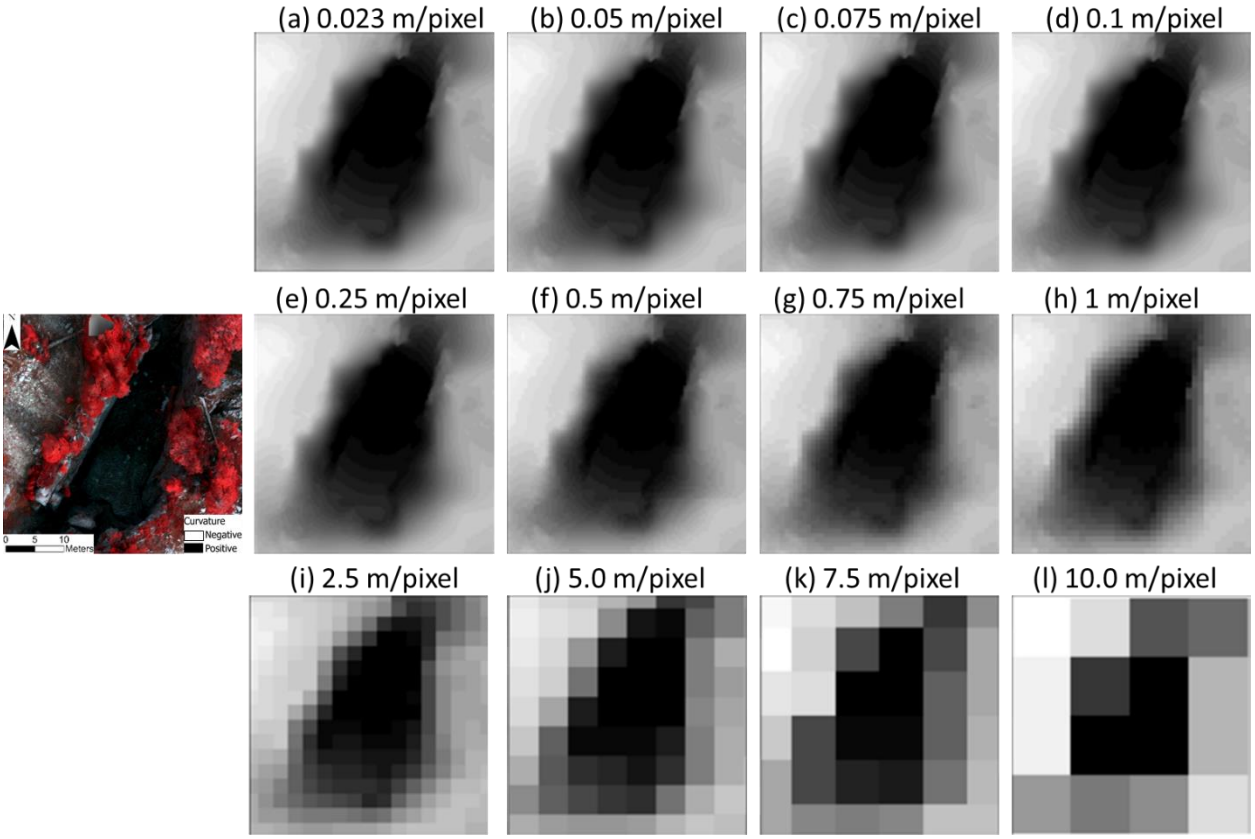

Figure 19: RGB data clipped to area of a known large karst feature (left) compared to the results of aggregating the resolution of the DTM for Polygon 2 with the resolution specific to each figure noted above.

Curvature calculations were able to be completed for the whole of Polygon 2 by using the data aggregated to a 1-meter resolution (Figure 20). Completing curvature calculations for the entire polygon allowed the results of this method to be visualized for a more expansive area that included a more comprehensive range of surficial karst sizes. The success of this method was determined by the calculations producing a nonlinear area of positive curvature encircled by negative curvature. Through further testing of the Weickert parameters at the 1-meter resolution, it was found that using default parameters (T=5, dt=1) worked best at reducing undesirable noise while providing the best possible signature of karst features (Figure 20c). Still, there was enough noise that identifying karst features through curvature calculations alone was not possible for all sizes of karst features. Additionally, some signatures mimicked a karst feature where there did not appear to be one. This method was found

useful, but it would need to be combined with another method to predict karst locations more accurately.

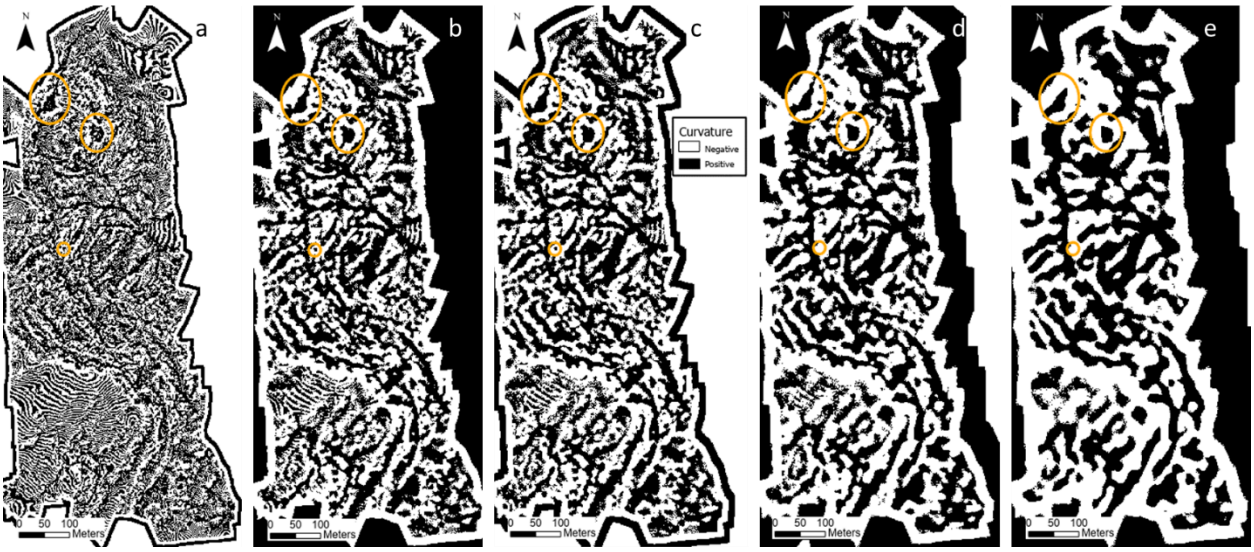

Figure 20: Curvature comparison for Polygon 2 at 1-meter resolution, white/black = negative/positive curvature; T = 1, dt = 0.5 (a); T = 5, dt = 0.5 (b); T = 5, dt = 1 (c) T = 10, dt = 0.5 (d); T = 20, dt = 0.5 (e). Small, medium, and large karst features circled in orange.

Using watershed properties to identify karst features was investigated using the UAV DTMs with a 1-meter resolution. This analysis sought to use sinks as pour points to delineate watersheds and as a method for identifying karst locations. Other studies have shown that fractures and bedding planes likely drain more surface water than karst openings (Ginsberg and Palmer, 2002). However, many surficial karst features represent surface locations that do not have another drainage outlet (e.g., sinkholes). Various neighborhoods, defined by the matrix size and shape used to calculate statistics for the central pixel, were used to run focal statistics properties in ArcGIS. Sinks were then located, and watersheds delineated using each of the resulting layers from running the focal statistics tool. After locating sinks, the results were examined, with the only difference between the resulting layers being neighborhoods used in the focal statistics step. Examining the results, it appeared that the rectangular neighborhood, with length and width dimensions of 3 x 3 and a statistic type set to mean, produced the best results (Figure 21). This was determined because there are sinks located when the rectangular

matrix is used with the focal statistic that other neighborhoods did not consistently identify (except for circular in a few cases). Additionally, there are also instances where using a rectangular neighborhood resulted in sinks being successfully located in visible pits/large fractures that are unmapped (Figure 21). There also appear to be occurrences with every focal statistic method used where sinks are placed amongst vegetation. In this instance, and with this data, the rectangular matrix appears to be best. However, more experimentation may be needed if these methods are applied to LiDAR data that does not include vegetation influences. In comparing the locations of pour points to sites of known surficial karst features, some pour points matched (or nearly matched) locales of known karst features, others did not (Figure 22). Because it is unlikely that all pour points represented locations of unmapped karst, this method needed to be combined with another method.

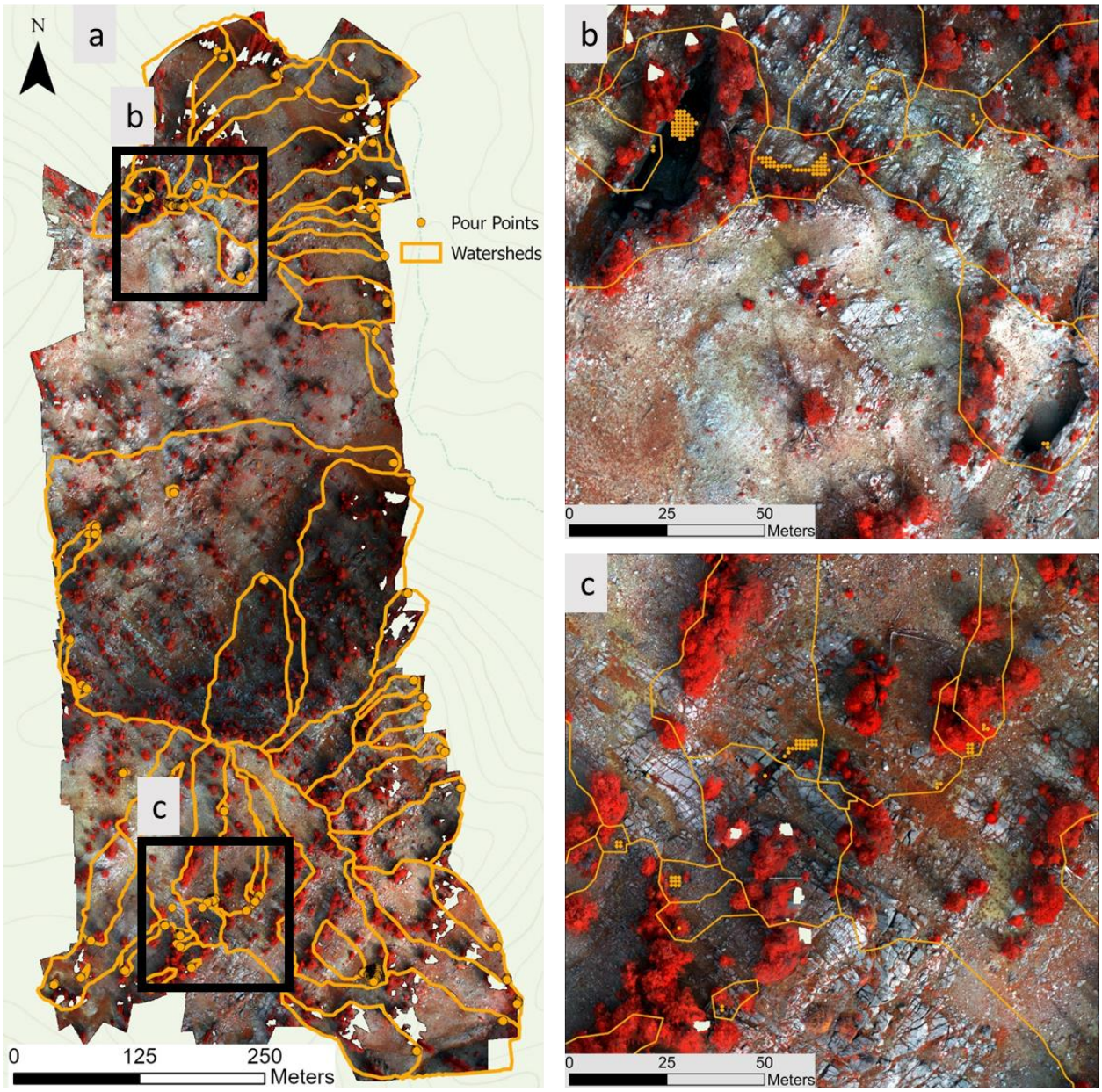

Figure 21: Results from rectangular 3 x 3 with a mean statistic type (a), with blow-ups of two areas within Polygon 2 to display accuracy of pour points predicting locations of surficial karst (b and c).

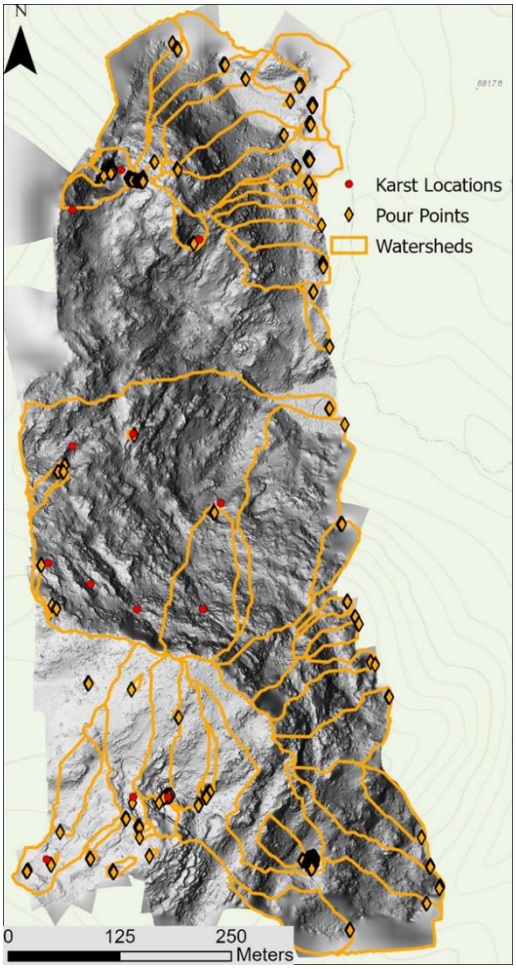

Figure 22: Known karst locations, calculated pour points, and delineated watersheds on a hillshade layer. Watersheds and pour points calculated using focal statistics with a 3 x 3 rectangular neighborhood used to calculate mean values.

Curvature calculations and locating sinks both were successful at detecting known karst features, as well as correctly predicting some sites of unknown karst. However, they also predicted locations where there do not appear to be sinkholes. Combining the results from these methods was a natural next step. Based on analysis using unclipped UAV DTMs at 1-meter resolution, the overlay/combination of curvature and sink location/watershed delineation provided additional evidence of likely locations of unmapped sinkholes (Figure 23). It is unclear what effects the removal, or presence, of vegetation has directly on these results.

Figure 23: Calculated pour points and delineated watersheds on top of a curvature layer. Watersheds and pour points were calculated using focal statistics with a 3 x 3 rectangular matrix used to calculate mean values. The curvature layer was calculated using T = 5 and dt = 1.

Discussion

Satellite data was used to visually compare known karst features to the surrounding areas and provided insight and promise that this study's hypothesis could be tested. It was also key in understanding that a resolution finer than 3 – 5 meters was needed to further test methods for identifying karst features (Figure 9). With that understanding, the UAV data was obtained and successfully provided the high-resolution data needed to test different potential methods (Figure 4). Additionally, the UAV data also provided further insight into the resolution needed to identify signatures (Figure 19).

With regard to the initial processing methods for the UAV data, there are some concerns that vegetation deletion and smoothing methods may have resulted in the removal of possible karst features. While both NDVI (Eqn. 1) and SAVI (Eqn. 2) were successful at identifying vegetation through reflectance values (Figure 10), the soil correction factor contained within the SAVI formula allowed for better isolation of vegetation. Therefore, the SAVI formula was ultimately used to sample reflectance values and remove vegetation (Eqn. 2, Figure 11). However, by simply eliminating vegetated portions of the study area, increased limitations to the utility of tested methods also resulted. Given that LiDAR data is uninterrupted by vegetation removal, it is thought that it will include additional success in method testing and is therefore recommended for future investigation.

The thermal assessment completed as part of the second analysis took advantage of detectable differences in temperature between known karst features and the surrounding area. These differences were known to exist from preliminary data collected within the study area (Figure 8). However, the success of identifying karst features was limited to areas that were in sunlight (Figure 12). There is no known reliable method for correcting the temperature of shaded areas without additional data. Additionally, a vegetation canopy would also affect thermal data, thereby making the detection of karst shrouded by vegetation unlikely. Because analysis of a thermal layer appears that it would require multiple flights to avoid shadows, resulting in a higher cost of data, it is thought to be a less desirable method at predicting surficial karst locations. The compilation of spectral and thermal analysis results showed that both masking methods had limited success at best and only limited search area (Figure 13). Still, combining methods and masking only to include areas both resulting layers had in common was more successful than either the spectral or thermal method alone.

Though image differencing succeeded at making some features of karst more prominent, this method failed to provide an identifiable signature for all three scales of karst features that were tested

(Figure 16). Edge detection was performed on the results of both smoothed images and images that utilized smoothing methods in combination with image differencing. Canny edge detection used in combination with Gaussian smoothing was found to produce a more complete edge outline around known karst features than when the Canny edge detection method was used in combination with moving average smoothing (Figure 17). Additionally, it was found that when Gaussian smoothing had an increased σ, undesirable noise was reduced; however, it also resulted in a more dashed edge around karst features (Figure 17d – f). The Canny method of edge detection is thought to have provided better results than other edge detection methods because, in addition to using strong detectable edges, it also uses weak edges connected to the strong edges (Gonzalez et al., 2009). In the end, using Gaussian smoothing, with σ = 16, in combination with Canny edge detection provided the best results (Figure 17e). Future studies may still find this method useful with additional adjustments of the parameters, using it in arrangement with additional layers, and/or in combination with machine learning.

Through using aggregated data to provide a range of resolutions, it was easy to see that even with the largest karst feature in Polygon 2, pixel resolution became too coarse by 2.5 meters per pixel to use curvature calculation as a method of identification (Figure 18i – l). Calculating curvature on aggregated data also showed that when the resolution was too fine, undesirable noise increased, making it harder to identify a signature of karst features. Based on those observations, it was determined that the ideal resolution existed between 0.5 and 2.5 meters per pixel (Figure 18 f – i). Using that understanding, Polygon 2 was aggregated to the resolution of 1-meter per pixel, and various parameters were tested for calculating curvature (Figure 20). It was found that when using spatial data that was clipped to a known karst feature, adjustments to the default Weickert parameters of T and dt were beneficial in enhancing an identifiable signature. However, when those changes to the parameters were applied to the whole of Polygon 2, it was found that those modifications did not work well with the wide range of scales that the karst features had within the study area. In the end, using default

parameters (T=5, dt=1) worked best at reducing undesirable noise while providing the best possible signature of karst features (Figure 20c). Still, there was enough noise that identifying karst features through curvature calculations alone was not possible for all sizes of karst features (Figure 20).

Because of concerns with noise and accuracy associated with using curvature results as a predictor, it was desirable to find another method of locating potential locations of karst that could be used in combination with the results from calculating curvature. With that in mind, watershed delineation and watershed properties were investigated as a potential method. Watersheds were successfully delineated using sinks as pour points (Figure 22). Through this method, it was found that the sink tool was useful in predicting locations of karst features (Figure 21). While some pour points matched (or nearly matched) locations of known karst features, others did not (Figure 22). Because it is unlikely that all pourpoints represented locations of unmapped karst features, this method needed to be combined with another method. Through combining results of methods used on aggregated data, it was found that using pour points and watersheds in combination with calculated curvature provided more evidence for likely locations of unmapped karst features (Figure 23).

This study has successfully identified promising methods that could be beneficial to future investigations. Future studies will likely have the most success by utilizing digital elevation data that does not contain a vegetative canopy. Data such as this is obtainable through LiDAR. With LiDAR data, future researchers should investigate edge detection, curvature, sink location, and watershed delineation. Adjustments to the Canny edge detection methods could provide a more desirable signature. Further adjustments to the Weickert smoothing parameters could provide added noise reduction when curvature is calculated. Also, supplementary analysis of 2-D curvature, as well as an investigation into 3-D curvature and planform curvature, may provide beneficial results. Using sinks and watershed delineation to predict locations of surficial karst features will also likely be more accurate

with the use of a more expansive dataset. That dataset should not include vegetation and should be clipped to the boundary of a larger watershed. Future investigations should keep in mind that these methods potentially deal with three resolutions or scales; first, the scale of the surficial karst opening; second, the resolution of the data being used; and third, the scale of the parameters being adjusted for each analysis. Future efforts could further investigate the relationships between these scales to collectively help locate and enhance karst feature signatures.

Conclusion

If there is one finding that surpasses all other findings in this study, it is that the presence and removal of vegetation poses a problem to successfully locating surficial karst features. Therefore, future studies should utilize data that does not include vegetation. Limiting the search area based on thermal values was very successful in sunlit areas. However, if thermal data is to be used in future studies, additional data will likely be required. Though edge detection was explored, it did not provide an uninterrupted boundary around known karst features. At the time, it was thought that other methods could provide a more complete signature; therefore, it was not explored further. Looking back on this study, this method may have been dismissed too quickly and there could still be potential associated with a deeper study of utilizing edge detection methods to identify surficial karst. Future studies could explore edge detection further and use it in combination with other methods.

Calculating curvature was beneficial and provided a signature. However, depending on the data resolution, the scale of the surficial karst opening, and terrain characteristics, there are also false positives and locations where this method fails to predict known karst features. Future studies should explore this method further by adjusting other parameters associated with the Weickert method of smoothing and include an analysis of average curvature in the x and y direction, curvature of the principal orientation, planform, and 3-D curvature. Using sinks to predict the location of karst features

was successful. However, the UAV data resulted in sinks in locales where vegetation had been removed and in locations along the edges of the study area. Therefore, potential studies may have more success using this method with data that does not include vegetation and clipping a more expansive area to a watershed. Future studies will likely find the most success at predicting surficial karst locations by utilizing machine learning with the results of two or more methods to locate karst features.

References

Agisoft Metashape User manual, Professional edition, Version 1.6 LLC Agisoft - Agisoft LLC, St. Petersburg, Russia, from https://www.agisoft.com/pdf/metashape-pro_1_6_en.pdf

Bahr, K., (2016), Structural and Lithological Influences on the Tony Grove Alpine Karst System, Bear River Range, North Central Utah. All Graduate Theses and Dissertations. Paper 5015.

Ford, D. C., & Williams, P. W. (2007), Karst Hydrogeology and Geomorphology, Wiley, Chichester.

Goldscheider, N. (2005), Karst Groundwater Vulnerability Mapping: Application of a New Method in the Swabian Alb, Germany. *Hydrogeology Journal* vol. 13, 555–564. https://doi.org/10.1007/s10040-003-0291-3

Gonzalez, R. C., Woods, R. E., Eddins, S. L. (2009). *Digital Image Processing Using MATLAB*. 2nd ed., Gatesmark Publishing, 2009.

Hartmann, A., Barberá, J. A., & Andreo, B. (2017). On the Value of Water Quality Data and Informative Flow States in Karst Modeling. Hydrology and Earth System Sciences, [s. l.], v. 21, p. 5971–5985, 2017. doi:10.5194/Hess-21-5971-2017.

Hartmann, A., Goldscheider, N., Wagener, T., Lange, J., & Weiler, M. (2014), Karst Water Resources in a Changing World: Review of hydrological modeling approaches, Rev. Geophys., vol. 52, 218–242, doi:10.1002/2013RG000443.

Kresic, N., (2013). *Water in Karst: Management, vulnerability, and restoration*. New York: McGraw-Hill.

Logan River Observatory (LRO) (n.d.). "Sites and Infrastructure." *Utah State University*, Utah Water Research Laboratory, 2021, uwrl.usu.edu/lro/locations.

Lucić, I., Palmer, A., & Palmer, M. (2017), Interview with Arthur and Margaret Palmer - The Lessons We Learn from Living On Karst Can Be Extended Far Into Other Geologic Regions. *Acta Carsologica*, vol. 46, no. 2-3, 2017, pp. 141–148.

Luetscher, M., & Jeannin, P. Y. (2004) "Temperature Distribution in Karst Systems: The Role of Air and Water Fluxes." *Terra Nova*, vol. 16, no. 6, 17 Nov. 2004, pp. 344–350., doi: https://doi.org/10.1111/j.1365-3121.2004.00572.x.

MathWorks. "Edge Detection." *MATLAB & Simulink*, The MathWorks Inc, www.mathworks.com/help/images/edge-detection.html.

Neilson, B. T., Tennant, H., Stout, T. L., Miller, M. P., Gabor, R. S., Jameel, Y., et al. (2018). Stream Centric Methods for Determining Groundwater Contributions in Karst Mountain Watersheds. *Water Resources Research*, 54, 6708– 6724. https://doi.org/10.1029/2018WR022664

Planet Team (2017). Planet Application Program Interface: In Space for Life on Earth. San Francisco, CA. https://api.planet.com

Spangler, L. (2011). Karst Hydrogeology of the Bear River Range in the Vicinity of the Logan River, Northern Utah. *Geological Society of America Rocky Mountain-Cordilleran Section Meeting*.

Tyson, Conor. (2021). "Effects of Climate Forcing Uncertainty on High-Resolution Snow Modeling and Streamflow Prediction in a Mountainous Karst Watershed" M.S. Thesis. Utah State University. All Graduate Theses and Dissertations. 8041.https://digitalcommons.usu.edu/etd/8041

Utah Epscor. (n.d.). IUTAH - innovative Urban Transitions and Aridregion Hydro-sustainability. http://iutahepscor.org/

Wallace L, Lucieer A, Malenovský Z, Turner D, & Vopěnka P. (2016). Assessment of Forest Structure Using Two UAV Techniques: A Comparison of Airborne Laser Scanning and Structure from Motion (SfM) Point Clouds. *Forests*. 2016; 7(3):62. https://doi.org/10.3390/f7030062

Weickert, J. (1998). *Anisotropic Diffusion in Image Processing*. B. G. Teubner Stuttgart, 1998.